PRECLINICAL ALZHEIMER'S DISEASE IN THE ENTORHINAL AND TRANSENTORHINAL CORTEX

by

Sue Kulason

A dissertation submitted to The Johns Hopkins University in conformity with the requirements for the degree of Doctor of Philosophy

Baltimore, Maryland

December 2020

Abstract

Research on biomarkers of Alzheimer's disease has been shifting focus toward identifying changes in the preclinical stage, a stage prior to the emergence of cognitive deficits. Advances in the field of computational anatomy leverages noisy, longitudinal data for more sensitive and robust detection of shape differences. In particular, cortical thickness measures have been shown to be a sensitive marker of change. In this work, we introduce a pipeline for quantifying cortical thickness and develop three models to study the earliest changes detected from structural MRI. First, we investigate where grey matter atrophy occurs with great spatial resolution using a new cortical thickness metric and a mixed effects model of group differences. Next, we determine when grey matter atrophy begins using a piece-wise linear mixed effects model of atrophy. Finally, we characterize early progression of the disease in an individual using a subject-specific model of atrophy spread.

Primary Reader: Michael I. Miller, PhD

Secondary Reader: Laurent Younes, PhD

Acknowledgments

I would like to thank my mentor, Dr. Michael I. Miller, for his support throughout my graduate studies and for providing me the freedom to explore my areas of interest.

I would also like to thank my thesis committee members: Dr. Laurent Younes for his invaluable expertise in formulating mathematical models and statistical analyses; Dr. Arnold Bakker for sharing his clinical insights and expertise that shaped my thesis direction; Dr. Tilak Ratnanather for his depth of knowledge related to cortical thickness and interesting conversations; Dr. Alain Trouvé for his incredible mathematical expertise matched by his patience.

Thank you to all my colleagues at the Center for Imaging Science; Timothy Brown and Eileen Xu for their careful work segmenting the rhinal cortex; Anthony Kolasny for maintaining and upgrading computational resources used in this work; Daniel Tward and Kwame Kutten for advice and mentorship; to my lab mates for making CIS a fun place to work.

ACKNOWLEDGMENTS

Finally, I would like to thank my family and friends for their moral support throughout this journey. Thank you!

Sue Kulason

Baltimore, MD

November 2nd, 2020

Contents

List of Tables

List of Figures

Chapter 1

Introduction

1.1 Alzheimer's disease

Alzheimer's disease (AD) is a progressive neurodegenerative disease that typically occurs in old age, and is characterized by cognitive impairments such as memory loss. It is estimated that 5.8 million Americans live with AD today (in 2020), and that with the growth of the elderly population, this figure will rise to 13.8 million Americans by 2050.[1] Due to this large and increasing healthcare burden, there are now focused research efforts to understand the disease mechanism and develop effective treatments.

A classic sign of AD dementia is amnesia, or the inability to recall recent events and conversations. A more expansive list of clinical criteria for probable AD dementia includes:[2]

- impairment in one or more cognitive domains (for example, an impairment in

memory recall and visuospatial skills)

- a history of worsening cognition
- interference with completing functional tasks (for example, trouble paying their bills independently)
- a slow onset of symptoms that can span years
- exclusion of other causes of dementia (for example, vascular dementia)

Currently, AD can only be confirmed from a post-mortem identification of amyloid plaques and neurofibrillary tangles (NFT). Despite advances in neuropsychological assessments and diagnostic criteria, there remain issues with diagnostic specificity. Post-mortem analyses have revealed that 15 to 30% of people diagnosed with probable AD dementia show no evidence of AD histopathology.[3–7]

The issue is made more apparent earlier in the disease course. Years prior to a diagnosis of probable AD dementia, patients are often diagnosed with mild cognitive impairment (MCI). The clinical criteria for this diagnosis includes:[8]

- impairment in one or more cognitive domains
- concern from the patient or caretaker about a change in the patient's cognition
- maintainence of independence in completing functional tasks
- exclusion of other causes of cognitive impairment

- exclusion of a diagnosis of dementia

Post-mortem analyses have revealed that only 54% to 63% of MCI cases show AD histopathology.[9,10]

In addition to these issues with diagnostic specificity, there is accumulating evidence that toxic changes start to occur in the brain years before the onset of clinical symptoms.[11] Turning back to post-mortem histopathological evidence, we see that AD severity can be staged based on the location and concentration of NFT.[12–14] During Braak stage I, NFT are found only in layer II of the transentorhinal cortex (TEC). NFT accumulates in other layers and spreads medially to the entorhinal cortex (ERC) during Braak stage II. It has been noted in post-mortem analyses that Braak stages I and II typically show no evidence of any cognitive impairment.[12] Initial clinical symptoms do not typically occur until Braak stages III and IV, though there is a variable relationship between clinical staging and histopathological staging.[15–17] Braak stage III and IV are the limbic stages of the disease, as there is marked accumulation of NFT in limbic regions such as the hippocampus and amygdala.[12,18] The final stages of the disease, referred to as the isocortical stages, are marked by severe cortical destruction and NFT accumulation in isocortical association areas, such as the orbitofrontal cortex.[12]

How can researchers hope to study and treat a disease for which the patient population is hard to identify? First, a set of more stringent diagnostic criteria for research purposes have been proposed. For example, the accuracy of MCI diagnosis

is substantially higher in patients who exhibit an amnestic sub-type of MCI; these are patients who have an impaired ability to recall recent events and conversations. Researchers have also developed a number of biomarkers to aid in the specificity and sensitivity of AD diagnosis. This can be roughly divided into biomarkers from cerebral spinal fluid, and from imaging. One such promising biomarker is the β-amyloid level found in cerebral spinal fluid.[19,20] Unfortunately, abnormal levels of β-amyloid are also found in a number of other neurodegenerative diseases, including Lewy body disease, and can sometimes be found in cognitively healthy adults. It is likely that a combination of biomarkers and clinical criteria are needed to improve the specificity and sensitivity of identifying AD.

Imaging biomarkers of neuronal injury are well-positioned to 1) increase diagnostic specificity by determining if etiology is consistent with AD pathology, and 2) increase sensitivity by identifying populations at risk of converting to a symptomatic stage of the disease. There are three types of imaging that show promise for the development of neuronal injury biomarkers. Positron emission tomography (PET) with a glucose metabolic tracer measure metabolism and have been shown to differentiate between AD and frontotemporal dementia.[21] Single-photon computed emission tomography (SPECT) measures perfusion, and has also had some early success differentiating between AD and frontotemporal dementia. Structural magnetic resonance imaging (MRI) measure neuronal injury and have shown high specificity in identifying AD from brain tumors, vascular dementia, and non-neurodegenerative diseases. Faster

rates of volume atrophy and regionally-specific atrophy patterns as calculated from structural MRI have been used to predict conversion to MCI and AD.[22]

While the exact mechanism is not understood, NFT, particularly in the presence of amyloid plaques, are associated with spatially-specific decreased neuron counts and increased grey matter atrophy in AD.[23] The link between NFT and neurodegeneration is further strengthened by studies of frontotemporal dementia, which has shown that hyperphosphorylation of tau, critical for the formation of NFT, is sufficient to cause neurodegeneration.[24] In AD, NFT accumulation and other neuropathological changes are linked to neuronal injury starting in the rhinal cortex, which can be measured indirectly using structural MRI.[25,26] Cross-sectional studies have confirmed that entorhinal, hippocampal, and amygdalar atrophy detected from structural MRI is associated with both clinical disease severity and NFT concentration.[25,27–29]

More recently, MRI studies have detected atrophy that precedes the onset of clinical symptoms, often detecting these smaller changes using time-series data analysis[30–33] and survival analysis.[34–38] As MRI resolution and contrast have improved, research has turned to building techniques to identify biomarkers that are sensitive to grey matter atrophy and robust to brain shape variability. In this thesis we focus on measuring atrophy in the earliest site of change, the rhinal cortex. Throughout this work, we will refer to the rhinal cortex when discussing the TEC and ERC.

1.2 Computational anatomy

The field of computational anatomy has developed a framework for quantifying anatomical variability over populations and studying local shape changes. In this framework, neuroanatomy is represented as a Grenander deformable template, which is mapped elastically to a target using a non-linear diffeomorphism.[39,40] This type of diffeomorphic model was first applied to neuroanatomy by Beg to compute image mappings.[41]

Problem Formulation 1: Image matching with flows of diffeomorphisms

Given volume I in domain $\Omega \subset \mathbb{R}^3$, a Hilbert space V of vector fields on Ω such that $V \subset C_0^1(\Omega, \mathbb{R}^3)$, solve the constrained optimization problem:

$\arg\min_{v_t} \int_0^1 ||v_t||_V^2 dt \ + \ \lambda ||I_0 \circ \varphi_1^{-1} - I_1||_{L^2}^2$ subject to $v_t \in V$ and $\frac{\partial \varphi_t}{\partial t} = v_t \circ \varphi_t$

In this formulation, the space of diffeomorphisms is equipped with a distance metric based on the distance traveled along a velocity field, called a flow. Solving the constrained optimization problem outlined in Problem Formulation 1, the optimal diffeomorphism φ that maps template image I_0 to target image I_1 travels the shortest path, and is therefore referred to as a geodesic flow. The term $\int_0^1 ||v_t||_V^2 dt$ is referred to as the regularization term and enforces some properties of smoothness; the term $||I_0 \circ \varphi^{-1} - I_1||_{L^2}^2$ is referred to as the data-fidelity term and ensures the deformed template matches the target.

By equipping the space of diffeomorphisms with an appropriately smooth distance metric, we can perform large deformations that conserve a few nice properties for studying anatomy. For example, diffeomorphisms provide a one-to-one correspondence between points, allowing for direct comparisons of a location across subjects. Diffeomorphisms are also invertible, ensuring that once a mapping from a template to target is established, the inverse mapping can be used to transform from target back to the template space. Applied to neuroanatomy, this type of smooth, invertible, one-to-one mapping prevents the creation of undesirable holes and overlapping regions.

This diffeomorphic model has been further modified for surface matching applications using currents,[42] which are invariant to parametrization, and varifolds,[43] which are invariant to both parametrization and orientation. Surfaces reduce the complexity of shape representation and has been shown to have more robust mappings to noisy data than image volume representations.[44]

Problem Formulation 2: Surface matching with geodesic coordinates

Given surface S in domain $\Omega \in \mathbb{R}^3$, a Hilbert space V of vector fields on Ω such that $V \subset C_0^1(\Omega, \mathbb{R}^3)$, solve the constrained optimization problem:

$\arg\min_{v_t} \int_0^1 ||v_t||_V^2 dt \ + \ ||S_0 \circ \varphi_1^{-1} - S_1||^2$ subject to $v_t \in V$ and $\frac{\partial \varphi_t}{\partial t} = v_t \circ \varphi_t$.

The norm $||\cdot||^2$ on a surface S depends on the current or varifold method used.

These large deformation diffeomorphic metric mapping (LDDMM) techniques have been used to automatically map segmentations from a well characterized atlas to subjects[45,46] and to conduct population level studies of local shape changes in regions of the brain (e.g. hippocampus).[47,48] More recently, methods have been developed to incorporate longitudinal subject data to be more accurately and robustly map shape changes of an individual over time.[49]

1.3 Cortical thickness

A number of shape metrics have been used to assess neurodegeneration from structural MRI. The earliest studies began by correlating whole brain volume or ventricular volume with clinical disease severity. Later, studies turned to region-specific volume measures of the hippocampus, ERC, and amygdala. These were shown to be more sensitive than whole brain volume and ventricular volume.[36,50]

Volume is a composite measure of surface area and cortical thickness, which are phenotypically independent measures. While both measures influence volume, it has been shown that volume is more closely linked to surface area.[51] Since the human cortex is highly folded, it poses a challenge to accurately measure cortical thickness in regions of high curvature. Historically, volume measures have had the advantage over cortical thickness measures for being more robust to poor image quality and poor segmentation quality. However, as image quality and image analysis techniques

have improved, cortical thickness has become a primary candidate for detecting local, small changes in grey matter atrophy. Simply stated:

> "Hippocampal volume is the most widely employed and discussed measure of this type, and while clearly informative, it is increasingly appearing to be less sensitive and specific than other measures such as regional cortical thickness."[52]

Two computational paradigms exist for calculating cortical thickness: voxel-based methods and surface-based methods.[53] Voxel-based methods include the use of line integrals,[54] solving the Laplacian,[55] and diffeomorphic registration[56] (such as the DiReCT algorithm available through ANTS). While these volume-based methods are computationally efficient, surface-based methods have been shown to more accurate and robust to image resolution, field strength and scanner type.[57–59]

Surface-based methods start by estimating the grey matter-white matter (GM-WM) surface, the pial surface, or both surfaces. Often, there is a step to correct surface topology using smoothness constraints or intersection rules. It is intuitive to define cortical thickness as the distance traveled along an orthogonal projection from a point on one of these surfaces to the other surface. However, this type of approach is sensitive to noise and the choice of starting surface, particularly in highly folded regions.

A popular method made available through FreeSurfer deforms the GM-WM surface to the pial surface, then calculates distance as the average of the distance from the GM-WM surface to the closest point on the pial surface, and from that point

back to the closest point on the WM surface.[57] This simple method is more robust to noise, but has been shown to sometimes underestimate thickness.[60]

Another surface-based method is an adaptation of the volume-based Laplace method.[61,62] This method generates a point-to-point correspondence between the surfaces and has been shown to be more accurate and sensitive to diagnostic differences.[59]

Beyond point-to-point correspondence, further efforts have been made to develop techniques that are more biologically-inspired and anatomically meaningful.[63] It has been suggested that cortical layers are equivolumetric rather than equidistant.[64] That is to say, in areas of high curvature, outer layers are thinner while inner layers are thicker. One new surface-matching method, called normal geodesic flow, generates these equivolumetric lamina in addition to maintaining nice properties of anatomy such as invariance to surface parametrization, point-to-point correspondence, and intersection rules.[65]

1.4 Dissertation outline

We have now introduced the need for imaging biomarkers of neurodegeneration to improve specificity and sensitivity of identifying early AD. We reviewed spatially and temporally specific histopathology, with the rhinal cortex as the earliest site of disease-related changes. We then discussed a diffeomorphic framework of methods to

quantitatively compare brains, and in particular, emphasized the advantage of new cortical thickness methods.

The thesis is organized as follows. We first introduce a new pipeline for studying the cortical thickness of the rhinal cortex. The pipeline is largely based on the large deformation diffeomorphic metric mapping framework for studying anatomy. Next, we discuss two types of population-level analysis for studying the disease in high spatial resolution and high temporal resolution, respectively. We discuss the statistical framework for testing hypotheses about anatomy. Finally, we introduce a subject-specific model of disease spread that is based on our current understanding of atrophy in early AD.

The work discussed in Chapters 2, 3, and 4 have been adapted from the following publications:

- S. Kulason, D. J. Tward, T. Brown, C. S. Sicat, C. F. Liu, J. T. Ratnanather, L. Younes, A. Bakker, M. Gallagher, M. Albert, M. I. Miller, "Cortical thickness atrophy in the transentorhinal cortex in mild cognitive impairment." NeuroImage: Clinical, vol. 21, p. 101617, 2019.

- S. Kulason, E. Xu, D.J. Tward, A. Bakker, M. S. Albert, L. Younes, M. I. Miller, "Entorhinal and transentorhinal atrophy in preclinical Alzheimer's disease," Frontiers in Neuroscience, vol. 14, p. 804, 2020.

- S. Kulason, M. I. Miller, A. Trouvé, "Reaction-diffusion model of cortical atro-

phy spread during early stages of Alzheimer's disease." bioRxiv, 2020.

Chapter 2

Pipeline for studying rhinal cortex morphology

A schematic of the pipeline for studying rhinal cortex morphology is shown in Figure 2.1. The pipeline has five major steps prior to statistical analyses, which will be covered in Chapter 3. The first step is to perform accurate manual segmentations of the rhinal cortex from all subject and atlas MRIs. Next, we estimate a surface averaged across the subjects, which is called a template surface. This step is referred to as template estimation. We then diffeomorphically map the template to each segmentation, utilizing longitudinal data to smooth variations in boundary definition. This unbiased longitudinal diffeomorphometry provides a point-to-point correspondence such that subjects can be quantitatively compared. From these surface mappings, we calculate cortical thickness using an approach called normal geodesic flow. Finally, we

diffeomorphically map atlases that have structural, functional, and histological subregional labels to the template surface. This allows us localize differences to subregional labels used in different fields.

2.1 Segmentation

The pipeline starts with a manual segmentation of the rhinal cortex using Seg3D software.[66] The ERC, otherwise known as Brodmann area 28, and TEC, or Brodmann area 32, are histologically well-defined regions. We approximate these boundaries using a set of structural markers visible on MRI. The boundaries of the ERC are defined on MRI as follows:

- Rostral: 4mm rostral to the most rostral tip of the hippocampal head
- Caudal: 2mm caudal to the gyrus intralimbicus
- Medial: as far as visible GM-WM boundary, which occurs lateral to the uncal notch
- Lateral: before entering the medial bank of the collateral sulcus

Similarly, the boundaries of the TEC are defined on MRI as follows:

- Rostral: 4mm rostral to the most rostral tip of the hippocampal head
- Caudal: 2mm caudal to the gyrus intralimbicus

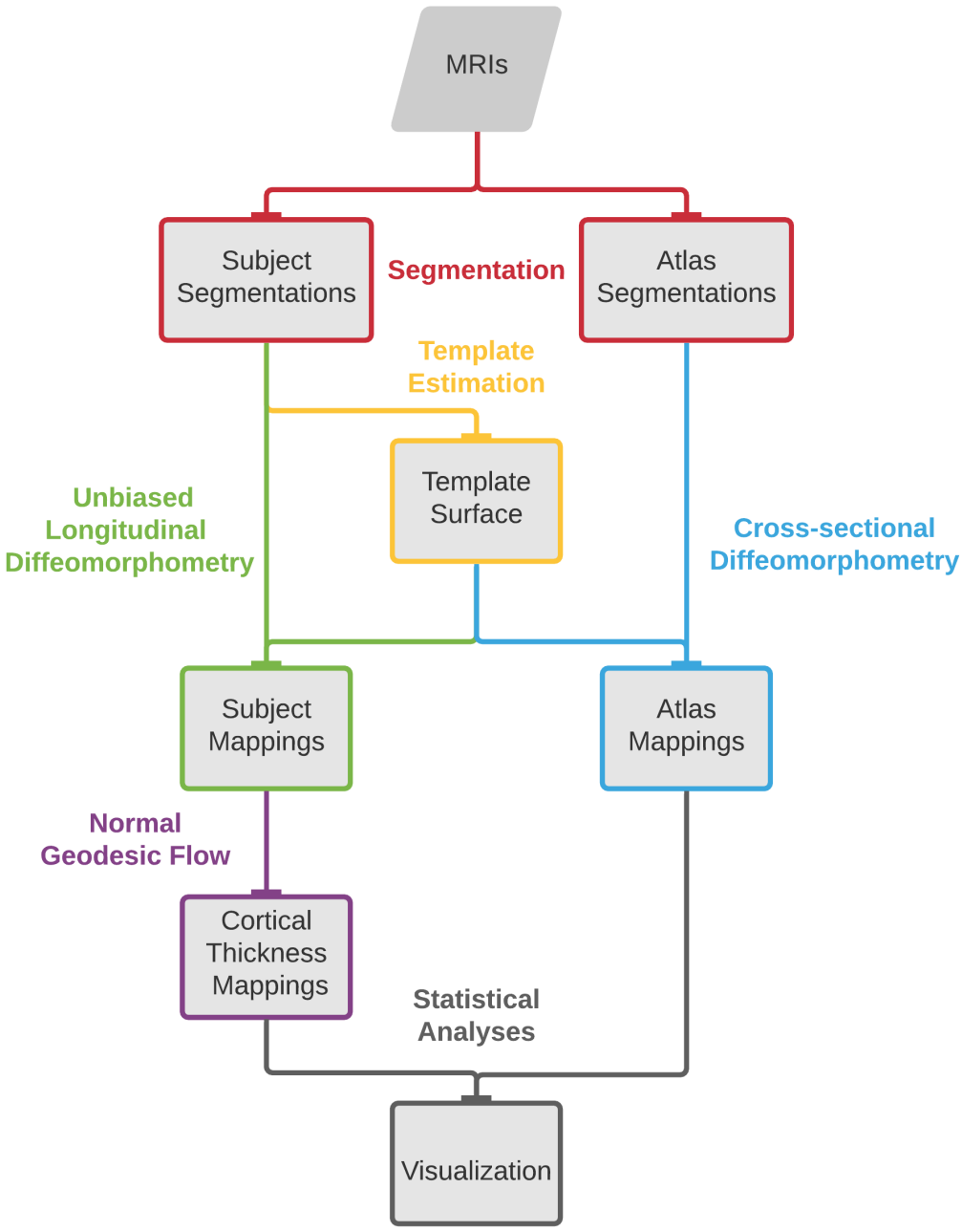

Figure 2.1: Schematic of the pipeline for studying rhinal cortex morphology

- Medial: the most medial extent of the collateral sulcus
- Lateral: deepest extent of the collateral sulcus

In histology, the anterior and posterior boundaries of Brodmann area 35 extend past and enclose Brodmann area 28. The boundaries of the TEC defined on MRI exclude these most anterior and posterior regions due to a lack of consistent visible landmarks. In particular, delineation of the ERC and TEC boundaries anterior to the hippocampal head is more complicated, even in histology. Originally, Insausti and colleagues designated this region to be a mix of ERC and perirhinal cortex (PRC),[67] whereas Krimer and colleagues defined this region as part of the primary olfactory cortex.[68] More recent work from Van Hoesen and colleagues suggests that this area is actually ERC.[69] Some of these discrepancies in reports may be due to the variable folding pattern in this anterior extent of the rhinal cortex. There are at least three folding variants of the rhinal sulcus, and the boundaries of the ERC are not well-defined based on folding patterns visible on MRI.[67] Given these difficulties, the roughly 5 mm region of cortex that is more than 4 mm rostral to the tip of the hippocampal head and typically anterior to the amygdala is excluded in our procedure.

The delineation of the ERC also excludes a small dorsal medial aspect of the ERC that rests against the amygdala. This corresponds to a portion of the intermediate superior subregion of ERC, as shown in Figure 2.2. Since this region of the ERC is indistinguishable from the amygdala on T1 MRI scans, the exclusion of this region is standard in MRI ERC delineation.[71,72]

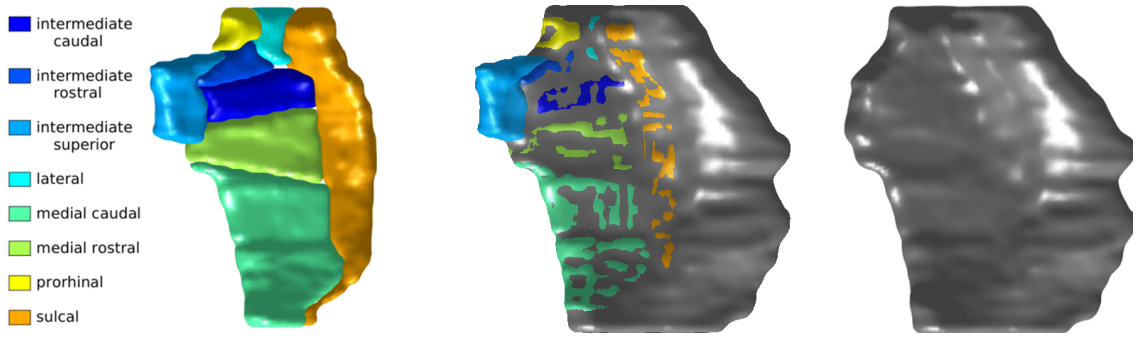

Figure 2.2: Overlay of histological definition of ERC with structural definition of rhinal cortex. Figure reproduced with permission.[70]

The lateral extent of the ERC that meets the medial extent of the TEC was defined based on histology of deep continuous collateral sulci (CoS).[67] Similarly, the lateral extent of the TEC was defined based on the histology of deep continuous collateral sulci.[69] This is important because the extent of the ERC and TEC depend on the variant of CoS,[67] and there are several anatomical variants to consider.[69,73] Figure 2.3 illustrates the three major anatomical variants of CoS. The following is an excerpt that describes these variants:[70]

> "The first variant is a deep, continuous sulcus where the rhinal sulcus shares a sulcal bed with the collateral sulcus proper. This variant has been referred to as Type I CoS[69] and Type II/Type III rhinal sulcus.[73] The second variant is a discontinuous CoS where the collateral sulcus proper begins posterior to the GI. This variant has been referred to as a Type IIa CoS[69] and Type I rhinal sulcus.[73] Finally, there is a variant with a discontinuous CoS where the collateral sulcus proper begins anterior to the [gyrus intralimbicus]. This variant has been referred to as a Type IIb CoS[69] and also falls into the category for Type I rhinal sulcus.[73]"

Type I and Type IIa CoS are of regular (between 1 and 1.5 cm) to deep (> 1.5cm) CoS length. In a deep CoS, the ERC extends up to the medial bank and the TEC

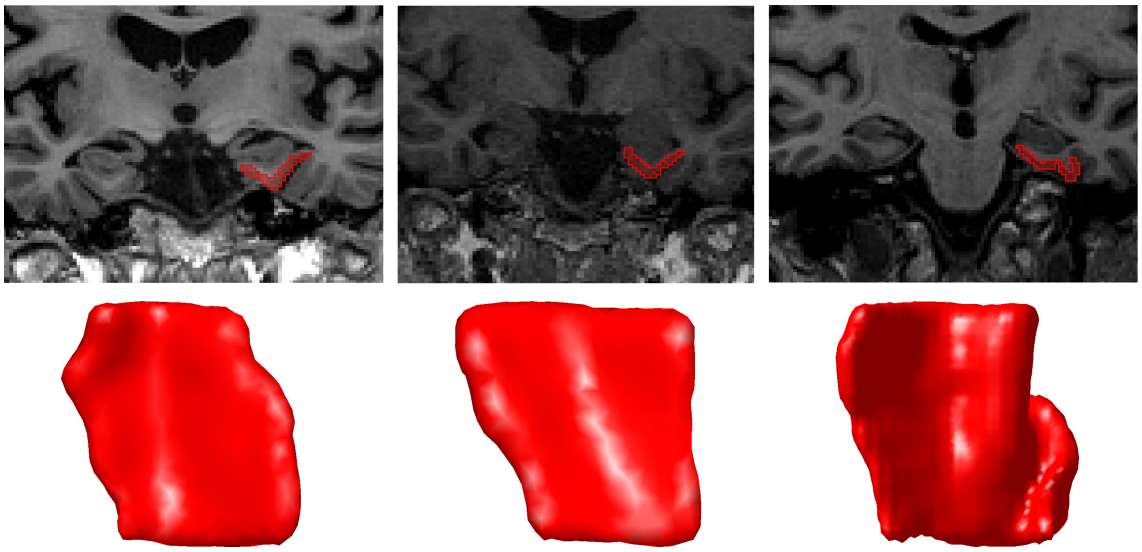

Figure 2.3: A coronal MRI section and corresponding surface of each CoS variant Type I (left), Type IIa (middle), and Type IIb (right). The surfaces are oriented such that left is medial, right is lateral, top is posterior, and bottom is anterior. Figure reproduced with permission.[70]

extends to the deepest extent of the CoS. In a CoS of regular length, the ERC extends to the midpoint of the medial bank of the CoS, and the TEC stops short of the deepest extent. In a shallow CoS ($<$ 1cm), as typically seen in Type IIb CoS variants, the ERC extends to the deepest extent of the CoS. The TEC is then on the lateral bank of the CoS. In order to study disease-related changes, we chose to reduce variability in anatomical differences by excluding Type IIb CoS.

2.2 Population surface template estimation

Once accurate segmentations of the rhinal cortex are generated for each subject and their multiple scans, the next step is to generate a population average, called the template surface. Here, we use an approach that was developed on the large deformation diffeomorphic metric mapping framework to calculate a Fréchet mean diffeomorphism for a population.[74]

We start by rigidly registering the segmentations to a hypertemplate. Previous works have selected a segmentation from the population to serve as the hypertemplate segmentation, which may bias the final template toward the selected subject. Instead, we rigidly register the segmentations and take their Euclidean average to generate a hypertemplate segmentation. For each segmentation and the hypertemplate, a smooth surface is generated in the following way: 1) apply Gaussian blur with a kernel size of 1 mm to the segmentation image 2) upsample the image using linear interpolation 3) generate an isosurface using marching cubes 4) remove undesirably narrow and small faces using Delaunay triangulation.[75]

A randomly selected subset of surfaces, including all time points, are then used to generate the template. While all surfaces can be used in this step, the task is computationally intensive with little added benefit for each additional surface. Random selection is important so that the template surface reflects the population. The

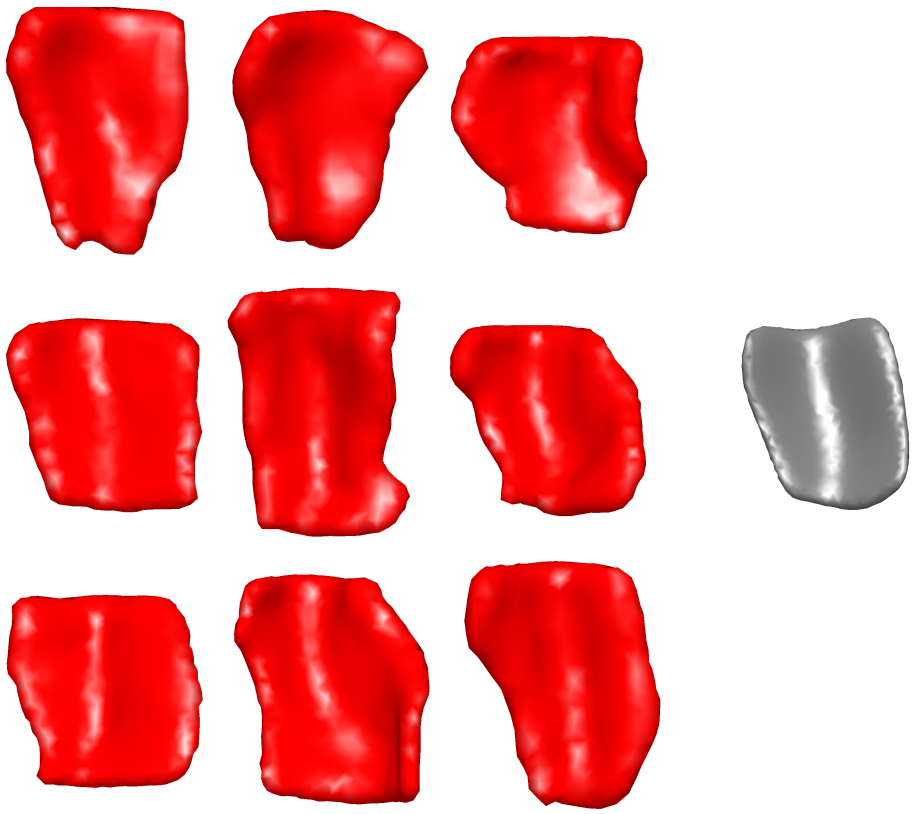

Figure 2.4: Example rhinal cortex surfaces in red. The resulting population surface template in grey. The surfaces are oriented such that left is medial, right is lateral, top is posterior, and bottom is anterior. Figure reproduced with permission.[70]

hypertemplate surface is used as a prior to calculate the template surface.

We solve the Bayes problem of parametric surface-matching to estimate an initial momentum and associated diffeomorphism used to deform the hypertemplate. Note that the resulting deformed hypertemplate is the template surface. We estimate the diffeomorphism that follows a geodesic flow from the hypertemplate to template, and also minimizes the sum of geodesic flows from the template to each of the individual subject surfaces. This can be interpreted as a Fréchet mean diffeomorphism of the population. Details on the numerical implementation, which uses a mode approxi-

mation expectation-maximization algorithm is described by Ma et al.[76] This mode approximation is also the maximum a posteriori solution of the Bayes problem. Figure 2.4 shows a sample of rhinal cortices and the resulting template surface using this approach.

2.3 Subject mappings via unbiased longitudinal diffeomorphometry

At this point, we have a template surface and a set of segmentations of the rhinal cortex. For each subject's set of segmentations, we use a method called unbiased longitudinal diffeomorphometry to calculate surface mappings with points that correspond to each point on the template surface. This method defines an inexact matching problem for geodesic positioning, with a matching term between the dense interior of the transported template and the target segmentation. The problem formulation is different from the image-matching and surface-matching problems introduced in Chapter 1 since this method uses images for the data attachment term, but singular geodesic coordinates for the regularization terms. The new problem formulation is shown in Problem Formulation 3.

Problem Formulation 3: Matching with singular geodesic coordinates

Given a template segmentation image I_0, a set of target segmentation images I_1^i (for index $i \in 1, 2, 3...$) in domain $\Omega \in \mathbb{R}^3$, and a Hilbert space V of vector fields on Ω such that $V \subset C_0^1(\Omega, \mathbb{R}^3)$, which has an associated RKHS kernel $K \in \mathbb{R}^3 \times \mathbb{R}^3$, solve the constrained optimization problem:

$\arg\min_{p_0^0, p_0^1, t^*} ||p_0^0||_{V^*}^2 + \sum_{i=1}^{N} \lambda_0 \left(||p_0^1(t_i - t^*)||_{V^*}^2 + \lambda_1 ||I_0 \circ \varphi_{t_i}^{-1} - I_1^c||_{L^2}^2 \right)$ subject to $v_t \in V$, $\frac{\partial \varphi_t}{\partial t} = v_t \circ \varphi_t$, and $v(\cdot) = \int_U K(\cdot, f(u)) p(u) \partial\eta(u)$ for geodesic singular coordinates $p : U \to \mathbb{R}^3$ with surface representation $u \in U \subset \mathbb{R}^2$.

p^0 corresponds to the flow from template to target at time $t = t^*$, and p^1 corresponds to the flow from target at $t = 0$ to target at $t = 1$.

The approach deforms the template to a subject-specific average surface following a geodesic flow, and then follows a second geodesic trajectory to deform from this subject-specific average through all the segmentations of this subject. See Figure 2.5 for an illustrative example. The numerical solution for the maximum a posteriori is achieved by gradient descent using an adjoint method. The subject-specific average surface, mapped surfaces, and time t^* at which the subject-specific average surface is inserted into the second trajectory, are updated iteratively. Because this is a solution to a Bayes problem of parametric mapping, we have the advantage of filtering noisy boundaries introduced from manual segmentations over a series of scans. Details on this implementation are described by Tward et al.[49,78]

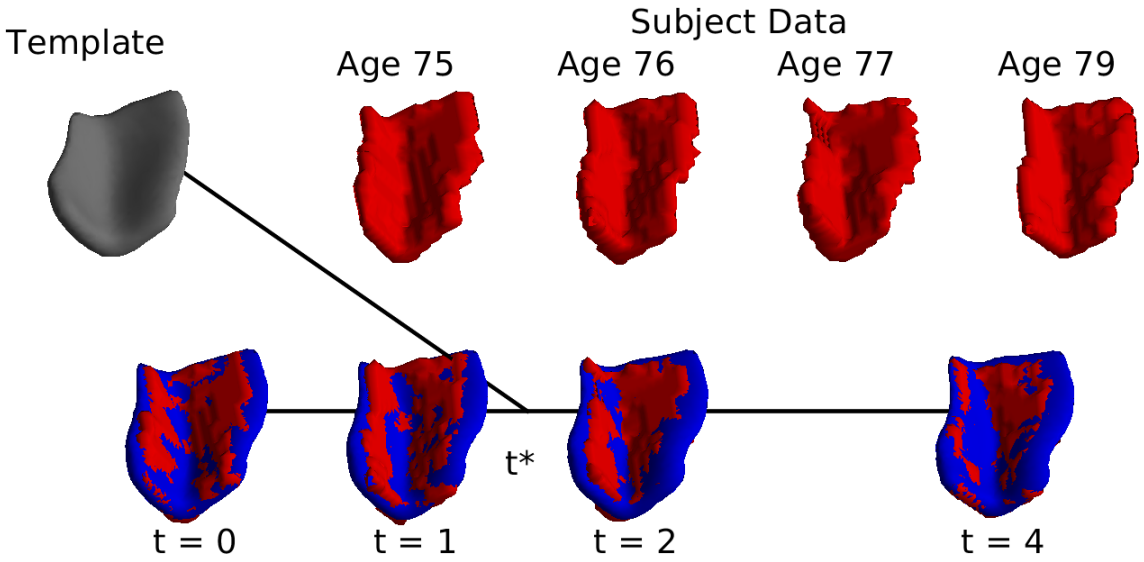

Figure 2.5: Schematic for performing unbiased longitudinal diffeomorphometry given a set of subject segmentations (red), a population surface template (grey) resulting in diffeomorphic mapping (blue). Figure reproduced with permission.[77]

2.4 Cortical thickness via normal geodesic flow

To calculate vertex-wise cortical thickness, we start by cutting the rhinal cortex template surface into two surfaces: one pial surface and one GM-WM boundary surface. Since the surface mappings from unbiased longitudinal diffeomophometry have a one-to-one vertex correspondence with the template surface, we can transfer this cut to all surfaces.

The pial surface, or outer surface, is then deformed to the GM-WM boundary surface, or inner surface, using an approach called normal geodesic flow.[65] The resulting mapping is constrained such that the flow remains normal to the evolving surface,

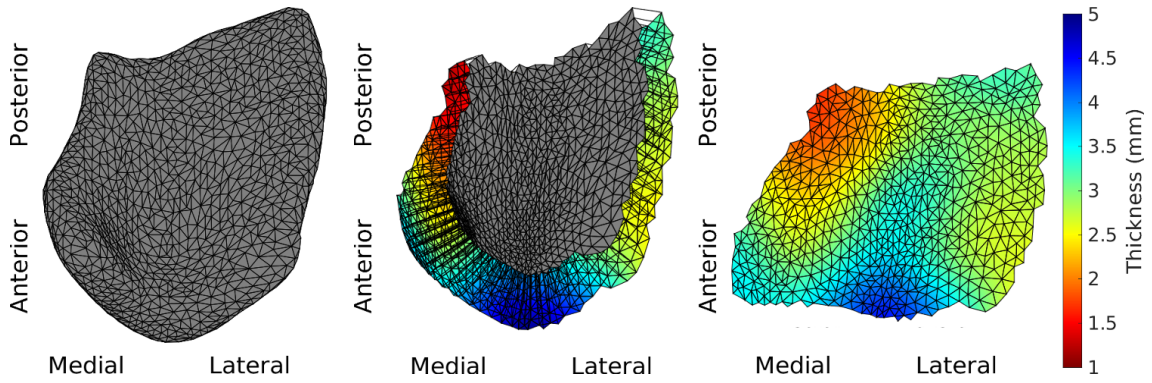

Figure 2.6: Schematic for calculating cortical thickness. Cut the surface (left), perform normal geodesic flow (middle), calculate distance traveled along trajectories (right). Figure reproduced with permission from.[77]

as shown in Problem Formulation 4. Details on how the data attachment term is invariant to surface parametrization is described by Ratnanather et al.[65]

Problem Formulation 4: Surface-matching normal to evolving surface

Given template surface S_0, target surface S_1 in domain $\Omega \subset \mathbb{R}^3$, a Hilbert space V of vector fields on Ω such that $V \subset C_0^1(\Omega, \mathbb{R}^3)$, solve the constrained optimization problem:

$\text{argmin}_v ||v_t||_V^2 + \int_S \lambda |Dv|_F^2 d\sigma_S + ||S_0 \circ \varphi_1^{-1} - S_1||^2$ subject to $v_t \in V$, $\frac{\partial \varphi}{\partial t} = v_t \circ \phi_t$, and $\partial_t S(t) = v(t, S(t))$ remains perpendicular to the evolving surface.

σ_S is the volume of S, Dv is the differential of v, and norm $||S||^2$ is chosen to be invariant to parametrization.

Finally, cortical thickness is calculated as the distance traveled along these trajectories. An illustration normal geodesic flow on a template surface is shown in Figure

2.6. Here, the color represents cortical thickness at each vertex on the pial surface.

2.5 Atlasing

Studying the rhinal cortex is complicated by inconsistent nomenclature of the region. The transentorhinal cortex on the medial bank of the CoS is often grouped together with the ectorhinal cortex on the lateral bank of the CoS, and together referred to as the perirhinal cortex (PRC).[67,72] Notably, this definition of PRC is different than the PRC of mouse brain atlases, where the label PRC refers specifically to the TEC and no surrounding regions,[79].[80] The Desikan-Killiany human brain atlas, available through FreeSurfer, refers to the ERC and TEC together as the ERC, and a caudal portion of the ERC as the parahippocampal gyrus.[71] In other atlases, the ERC, TEC, ectorhinal cortex, and parahippocampal cortex (PHC) together are referred to as the parahippocampal gyrus,[81].[82] While efforts are under way to standardize the naming scheme for the regions of the hippocampal formation, work on standardizing the nomenclature and borders of the rhinal cortex have not yet been approached.[83]

To address this, the final step in this rhinal cortex pipeline is to map several commonly used atlases to the template surface. Each atlas is manually segmented following the segmentation protocol described in Sectoin 2.1. A smooth surface is generated, and each vertex is assigned a subregional label using linear interpolation. The template surface is then mapped to each atlas surface by solving the standard

surface-matching problem.

We now show a particular use case that compares four different subregional sets of labels : 1) manual labels of ERC and TEC based on cortical folding seen in structural MRI[78] described in Section 2.1, 2) automated labels of ERC and parahippocampal gyrus (PHG) based on cortical folding seen in structural MRI[71] generated from FreeSurfer, 3) labels of posterior medial ERC (pmERC), anterior lateral ERC (alERC), and perirhinal cortex (PRC) based on connectivity patterns seen in functional MRI after manual segmentation of ERC in structural 7T MRI,[72] and 4) histological labels of intermediate superior ERC, intermediate rostral ERC, intermediate caudal ERC, prorhinal ERC, medial rostral ERC, medial caudal ERC, lateral ERC, sulcal ERC and TEC as identified in an 11T ex vivo MRI.[68,84]

The manual segmentation of ERC and TEC were performed on a scan with a Type IIa CoS variant of regular depth (1.30 cm). FreeSurfer 6.0 run with the Desikan-Killiany atlas was used to generate automatic labels on this same scan. The functional MRI atlas was also on a subject with Type IIa CoS variant of regular depth (1.20 cm).[72] Finally, the ex vivo MRI atlas was on a subject with a Type IIb CoS variant of shallow depth (0.75 cm).

In this ex vivo case, since the CoS was shallow, we extended the TEC to the lateral bank of the CoS, as seen in histology.[67,69] Atlas labels were mapped to the manually-defined rhinal cortex surface by linear interpolation. Finally, we diffeomorphically mapped the surfaces and their labels to the template surface in the large deformation

diffeomorphic metric mapping framework.[41] The result are four sets of labels– one from each atlas–at each vertex of the template surface.

We now provide some commentary on differences between the atlases. Regarding the anterior boundary of the ERC, the Desikan-Killiany atlas defined it at the rostral end of the CoS; this is approximately 6 mm anterior to the boundary defined in our own protocol. It includes the region with rhinal sulcus variants that are anterior to the amygdala, which was previously discussed in Section 2.1. On the other hand, the functional MRI atlas defined the anterior boundary at the rostral end of the amygdala, which coincided with the boundary of our protocol. The anterior boundary on the ex vivo MRI atlas was 0.5 mm posterior to the boundary from our protocol.

The posterior boundary of the Desikan-Killiany atlas was also dissimilar to the other atlases. The Desikan-Killiany atlas defined the posterior boundary at the caudal end of the amygdala. From histology, the ERC continues further posterior, running under and lateral to the hippocampal formation.[67–69] The functional MRI atlas defined the posterior boundary at the caudal extent of the CoS. Since this atlas is a Type IIa CoS variant, the caudal extent of the CoS coincided with 1.2 mm posterior to the GI, or one 0.6 mm slice anterior to the boundary described in our protocol. Similarly, the posterior boundary of the ex vivo atlas was 1.0 mm anterior to the boundary from our protocol. Again, we see somewhat similar boundaries in the functional MRI, ex vivo MRI, and our own protocol.

The atlases typically were in agreement about the medial boundary of the ERC.

The Desikan-Killiany atlas, functional MRI atlas, and our protocol had the medial boundary extended to where gray/white boundary was visible in the MRI. The ex vivo atlas, on the otherhand, also included the dorsal medial aspect of the ERC that lies medial to the amygdala. While visible on this high-field strength, this is a border that is not consistently visible on 3T T1 MRI.

Finally, the lateral extent of the ERC was somewhat variable between atlases. The Desikan-Killiany atlas extended to the most lateral extent of the CoS. This boundary definition closely follows the histological boundary of subjects with a shallow CoS variant,[67] often seen in Type IIb CoS. The functional MRI atlas, on the other hand, extended to the shoulder of the CoS. This is a definition that most closely resembles the histological boundary for a deep CoS variant.[67] Our protocol also follows a delineation that matches a deep CoS variant. Since the atlas had a regular CoS depth, it is likely that the ERC histologically ends somewhere between the should of the CoS and its deepest extent. In the following chapters, we analyze subjects that range from regular CoS depth to deep CoS depth and exclude subjects with a shallow CoS.

2.6 Experimental results

We now show a set of results produced using the rhinal cortex pipeline. We examined a set of preclinical subjects who were enrolled with normal cognition, and then converted to a diagnosis of MCI a year or more after their initial scan. A

description of the stringent diagnostic criteria used to identify these subjects is taken from an excerpt of our recent publication:[70]

> "Subjects were selected from the ADNI database (adni.loni.usc.edu). The criteria for stable NC included the absence of a diagnosis of MCI or AD on all baseline and follow-up visits, a CDR score of 0 on all baseline and follow-up visits, evidence of performance within the normal range on the Logical Memory Subtest of the Wechsler Memory Scale on all baseline and follow-up visits (based on education adjusted norms), and negative results for elevated amyloid β levels on the baseline visit (greater than a cut off of 192 pg/mL from CSF as established by the ADNI Biospecimen Core).
>
> The criteria for NC to MCI converters included evidence of performance within the normal range on the Logical Memory Subtest of the Wechsler Memory Scale at baseline (based on education adjusted norms), a CDR score of 0 on the baseline exam, a diagnosis of NC at baseline, and a diagnosis of MCI or dementia at a subsequent follow-up visit. Estimated MCI age-of-onset was established based on annual assessment of diagnosis. Note that subjects missing a diagnostic evaluation more than a year prior to MCI diagnosis were excluded, and one subject with an MCI diagnosis was also excluded due to a stable, high score on the Logical Memory Subtest of the Weschler Memory Scale five years after diagnosis.
>
> In addition, subjects had to have a minimum of three 3T MRI scans over two or more years. Out of the 30 subjects that met all criteria for NC to MCI converters, all subjects were examined and 17 had a continuous collateral sulcus (CoS) and were included in this study. We examined a subset of available stable NC subjects to reach a total sample size of 50. Out of the 84 subjects that met all criteria for stable NC, 68 were examined and 33 had a continuous collateral sulcus and were included in this study."

In addition to controls with NC and NC to MCI converters, we examined a group of subjects enrolled with MCI that later converted to a diagnosis of dementia (DEM). The criteria for MCI to AD converters included evidence of impaired performance on the Logical Memory Subtest of the Wechsler Memory Scale (based on age and education adjusted norms), a score of CDR ≥ 0.5, amyloid β positive, a diagnosis of MCI

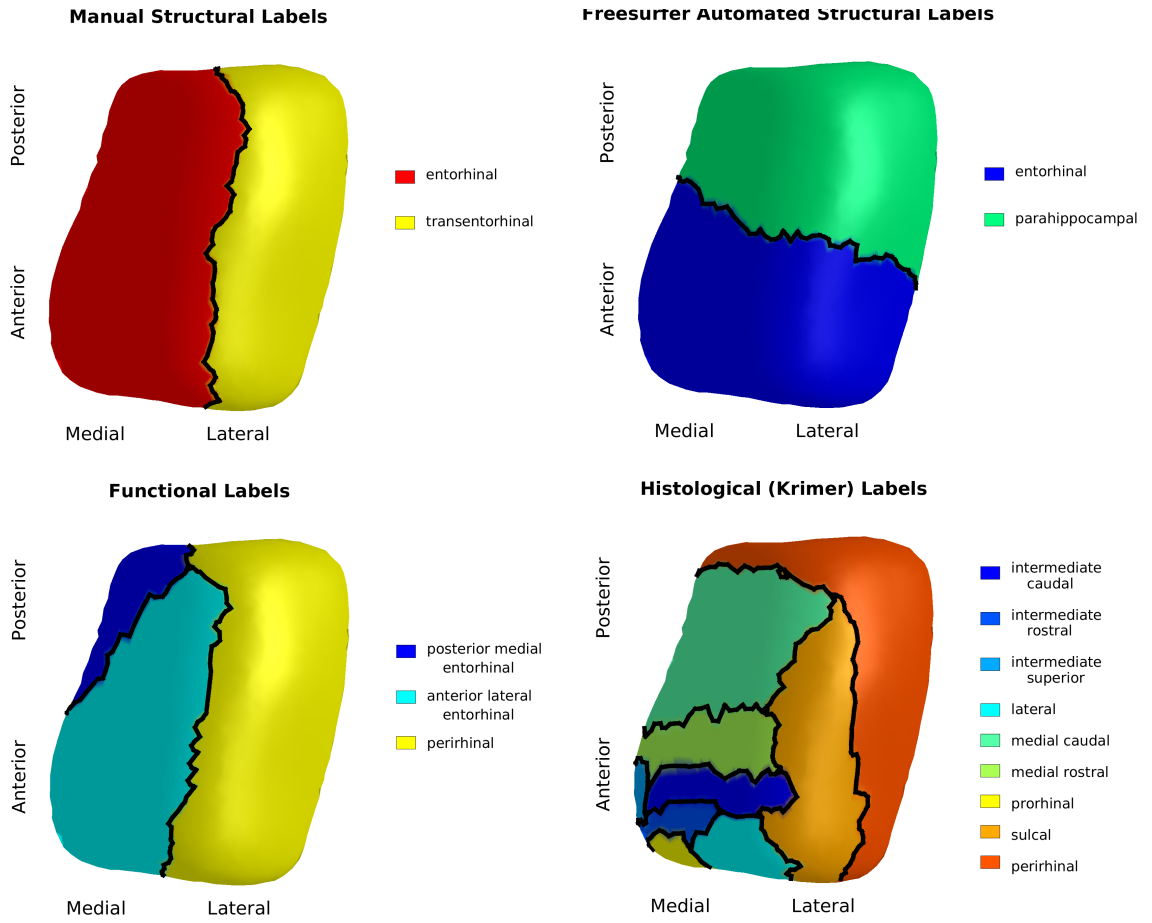

Figure 2.7: Manual structural labels (top left), automated structural labels (top right), functional labels (bottom left), histological labels (bottom right) mapped onto the population template. Figure reproduced with permission.[70]

at baseline, and a diagnosis of dementia during a follow up assessment. Estimated age-of-onset of Alzheimer's dementia was established based on annual assessment of diagnosis, and subjects missing a diagnostic evaluation more than a year prior to DEM diagnosis were excluded. Out of the 81 subjects that met all criteria for MCI to DEM converters, 50 were examined, and 19 had a continuous CoS and were included in this analysis. In total, 69 subjects and 303 3T MRI scans were analyzed.

To discuss the rhinal cortex morphology, we start by introducing subregional labels from the four atlas mappings, shown in Figure 2.7. Note how Desikian-Killiany's ERC extends further laterally than the other atlases, and that the posterior medial entorhinal cortex is a small functional subregion of the ERC. Average ERC and average TEC cortical thickness metrics were calculated based on the labels shown in the manual structural labels. These averages are plotted by age and diagnostic grouping in Figure 2.8.

The TEC is slightly thicker than the ERC, which is in agreement with our previous work.[85] In both the average TEC and average ERC, organization by MCI diagnosis date show cortical thickness measures decrease with progression of the disease, and that the rate of cortical thinning is noticeably steeper in NC to MCI converters than in stable NC subjects, and in MCI to DEM converters than NC to MCI converters.

Many past studies have focused on volumetric measures of Alzheimer's disease. For comparison, we calucate volume measures from the smoothed surfaces output from longitudinal diffeomorphometry, prior to surface cutting. Figure 2.9 shows the rhinal cortex volume measured for the set of subjects cortical thickness was shown in Figure 2.8. As with cortical thickness, volume measures decrease with progression of the disease, and the rate of thinning is steeper in NC to MCI converters compared to stable NC subjects, and steeper in MCI to DEM converters than NC to MCI converters. However, the average rate of change in stable NC subjects is steeper for volume (-1.6% per year) than for ERC or TEC thickness (-0.9% per year, -1.3% per

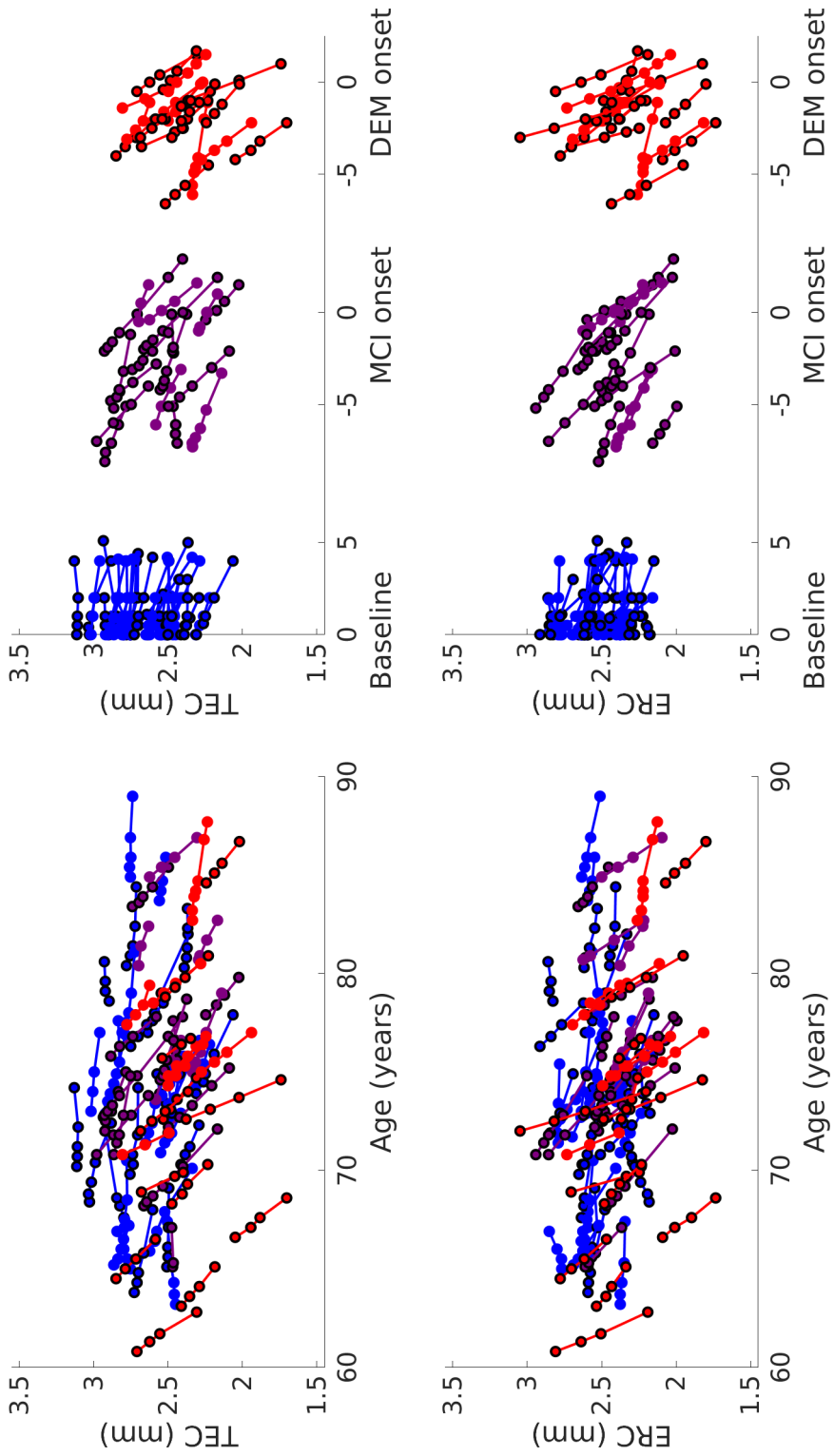

Figure 2.8: Average cortical thickness across the TEC (top) and ERC (bottom). Each line corresponds to a subject, the color to a diagnostic group (stable NC, NC to MCI, MCI to dementia), and the marker border to sex (no border is male, bordered is female).

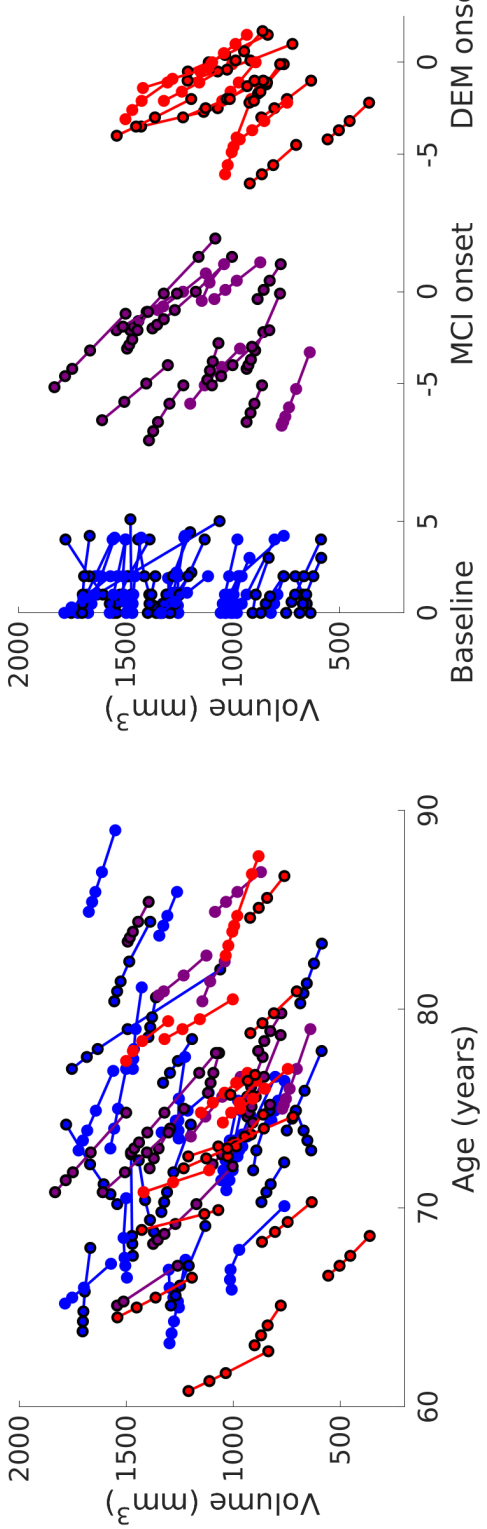

Figure 2.9: Average volume of the rhinal cortex (ERC and TEC together). Each line corresponds to a subject, the color to a diagnostic group (stable NC, NC to MCI, MCI to dementia), and the marker border to sex (no border is male, bordered is female).

year respectively). In addition, the range of natural variation in volume in stable NC subjects was 600 mm^3 to 1800 mm^3 (a factor of 3), compared to a cortical thickness range of 2.1 mm to 3.1 mm (a factor of 1.5) including both ERC and TEC. Given the milder effects aging and subject-to-subject variation, as well as the additional local information cortical thickness can provide, this type of thickness biomarker has potential to be more sensitive to disease progression than a volume biomarker.

2.7 Summary

Here, we have introduced a new pipeline for studying the morphology of the rhinal cortex. We started with manual segmentations based on anatomical landmarks visible in T1 MRI. This is because manual segmentations remain the gold standard and are preferred to automatic segmentations when the sample size is feasible. We then built smooth surface representations and estimated a template surface using a Bayesian surface-matching approach to construct an average diffeomorphism of the population. Building an accurate representation of the shape of a population is important to reduce bias. We mapped the template surface to longitudinal segmentation data for each subject, using an approach involving singular geodesic coordinates and image-matching. This approach allowed us to map each subject to the template coordinate space, and reduce variability in rhinal cortex boundaries within a subject. Cortical thickness was calculated by cutting the surface into an inner and outer sur-

face, which correspond to the GM-WM boundary surface and pial surface. Using a surface-matching approach with velocity constrained such that the surface evolves normal to the evolving surface, we estimate thickness as the distance traveled along trajectories from the outer to inner surface. Finally, a set of labeled atlases were manually segmented and mapped to the template surface to put various nomenclature from structural MRI, functional MRI, and histology into the context of our rhinal cortex morphological measures.

Beyond the experimental results shown for early AD, this pipeline has potential applications for studying other neurodegenerative diseases (i.e. Huntington's disease, frontotemporal dementia) and cortical changes that result from visual and hearing impairment. Statistical methods for quantifying differences in cortical thickness are covered in Chapter 3.

Chapter 3

Population-level analysis

We now develop a statistical framework for estimating where disease-related changes occur, and when these changes start to occur. We start by introducing a general framework of bootstrap resampling that can be used to test hypotheses and build confidence intervals. Next, we discuss specific use cases called group-wise difference analysis and change-point analysis. These analyses test where changes occur with high spatial resolution, and when these changes occur with high temporal resolution, respectively. This chapter has been modified, in part, from a publication related to this work.[70]

3.1 Bootstrap resampling approach

Let us consider a set of data where we are interested in studying whether variable x explains outcome y. Outcome y is known to be influenced by a second variable, z. For a concrete example, we can assign x as disease status, z as age, and y as cortical thickness. To test whether x explains y, we must build two models. One model represents the null hypothesis and is a function of z. The second model represents the alternative hypothesis and is a function of both x and z. We then test whether the fit of the alternative model is significantly better than the fit of the null model, which can be done using a likelihood ratio as the test statistic.

However, testing is complicated when outcome y is high dimensional. We deal with high dimensional data when examining vertex-wise cortical thickness measures. The introduction of such a large number of comparisons require careful statistical construction for controlling the probability of one or more false positives, called the family-wise error rate.

The most conservative approach is to correct statistics using a Bonferroni correction, which sets the threshold for significance based on the desired α level, and divides this by the number of comparisons made. However, this approach can be overly conservative in cases with a large number of positively correlated tests are performed, as seen in spatially-dependent metrics of cortical thickness.

On the other hand, non-parametric resampling-based methods can preserve spatial dependence and obtain an empirical estimate of the maximum test statistic distribu-

tion. This type of method makes no assumptions about the distribution and accounts for multiple comparisons by taking the *maximum* test statistic over the set. Spatial dependence is preserved by resampling across the surface. One neuroimaging review of statistical methods compared Bonferroni-related methods and resampling methods (as well as other methods) and found that:[86]

> "Non-parametric permutation and bootstrap methods provide estimation of the maximum distribution without strong assumptions, and without inequalities that loosen with increasing dependence. Only their computational intensity and lack of generality preclude their widespread use...with our real data studies the permutation method was found to be more sensitive [than Bonferroni or Random Field Theory] in all 11 data sets."

The difference between permutation methods and bootstrap methods is that permutation involves resampling under the null hypothesis *without* replacement, whereas bootstrapping involves resampling under the null hypothesis *with* replacement. Bootstrapping approximates the sampling distribution for exchangeability, where as permutation tests directly use the observed sampling distribution. As a result, bootstrapping makes fewer assumptions about the data and is a more general method that is applicable to a wider set of problems. However, bootstrapping is only valid asymptotically, whereas permutation testing, when justified, is exact for finite samples. Permutation tests have typically been structured by permuting the diagnostic labels. Instead, we choose residual boostrapping under the null hypothesis. Before resampling, we decorrelate the residuals from random effects using a whitening transformation. An example of a random effect is subject-specific differences, which is heterogeneous and cannot be explained by other variables. The underlying assump-

tion for bootstrapping is that the residuals being resampled are independent and identically distributed. Therefore, it is important to decorrelate the residuals. This procedure for hypothesis testing and building confidence intervals has been previously used with surface-based metrics.[87,88]

To conduct a hypothesis test, we bootstrap resample under the null hypothesis. For each bootstrap sample, the maximum test statistic over all the vertices is found and added to a distribution of maximum test statistics. The p-value associated with the hypothesis test is then the fraction of times the true likelihood ratio is smaller than a likelihood ratio obtained on the bootstrap samples.

We can calculate a confidence interval using a similar approach. Instead of using the null model to construct new samples, we now bootstrap resample under the alternative hypothesis. We then construct a distribution for each of the coefficients of interest and calculate the 90% confidence interval.

3.2 Group-wise difference analysis

In this section, we outline the construction of group-wise difference analysis using cortical thickness data and three diagnostic groups. The approach can be modified to use other shape metrics, and any number of groups larger than or equal to two. The diagnostic groups considered here are stable NC subjects, NC to MCI converters, and MCI to DEM converters. Note that the groups do not have to follow stages of one

particular disease, and can include separate disease etiologies.

Given a subject i, scan j, and vertex k, a log-linear mixed effects model under the null hypothesis can be written as Eqn (3.1). Note that in addition to age, the sex of a subject is known to influence cortical thickness:

$$\log(\text{thickness})_{i,j,k} = a_k + b_k \ \text{age}_{i,j} + c_k \ \text{sex}_i + e_{i,k} + \epsilon_{i,j,k}. \tag{3.1}$$

The vertex-wise coefficients a, b, and c, as well as the variance of e and ϵ are estimated by maximum likelihood. e is a subject-specific zero-mean Gaussian random effect. Age and the binary indicator variable for sex are fixed effects. ϵ is a zero-mean Gaussian that models noise.

The log-linear mixed effects model under the alternative hypothesis can be written as Eqn (3.2):

$$\begin{aligned} \log(\text{thickness})_{i,j,k} =& a_k + b_k \text{age}_{i,j} \\ &+ \left(a'_k + b'_k(\text{age}_{i,j} - \text{age\_MCIonset}_i)\right) \text{isPRE}_i \\ &+ \left(a''_k + b''_k(\text{age}_{i,j} - \text{age\_DEMonset}_i)\right) \text{isMCI}_i \\ &+ c \ \text{sex}_i + e_{i,k} + \epsilon_{i,j,k}. \end{aligned} \tag{3.2}$$

Here, a' is the mean difference in log cortical thickness at the time of MCI diagnosis in subjects that convert from NC to MCI. More specifically, this is the difference in thickness compared to subjects with stable NC. Similarly, a'' is the mean difference

in log cortical thickness at the time of DEM diagnosis for subjects that convert from MCI to DEM. Again, this difference is with respect to subjects with stable NC. b' and b'' corresponds to the disease-related rate of change in NC to MCI converters and MCI to DEM converters, respectively. These coefficients are all vertex-wise measures.

Now we introduce a short note on the notation used in these equations: isPRE is a binary indicator variable for whether a subject belongs to the group that converts from NC to MCI, and age_MCIonset is the age of MCI diagnosis. Similarly, isMCI is a binary indicator variable for whether a subject belongs to the group that converts from MCI to DEM, and age_DEMonset is the age of DEM diagnosis.

To discuss the likelihood function associated with these models, let us consider a more general form of the model, shown in Eqn 3.3:

$$Y = X\alpha + B\eta + \epsilon. \tag{3.3}$$

Given a set of data X (i.e. age, sex, and grouping) to explain Y (i.e. cortical thickness), and covariance matrix B (i.e. a mapping from scans to subjects), we estimate α, ρ^2 and σ^2. η and ϵ are independent, identically distributed zero-mean Gaussian random effects with a variance of ρ^2 and σ^2, respectively. Given I subjects and N scans in total, the likelihood function for this problem can be written as Eqn

3.4:

$$\begin{aligned} L(\eta, \alpha, \rho^2, \sigma^2 | X, Y) =& p(X, Y |\ \eta, \alpha, \rho^2, \sigma^2) \\ =& \prod_{n=1}^{N} \frac{1}{(2\pi\sigma^2)^2} \exp\left(\epsilon^T \frac{1}{2\sigma^2} \epsilon\right) \prod_{i=1}^{I} \frac{1}{(2\pi\rho^2)^2} \exp\left(\eta^T \frac{1}{2\rho^2} \eta\right). \end{aligned} \tag{3.4}$$

The likelihood function for our models can be simplified and written as a function of one variable, θ, defined as the ratio between σ^2 and ρ^2. We can then use MATLAB's 1D minimizer fminbnd (or fminsearch) to minimize the negative log likelihood function for each model, at each vertex. The negative log-likelihood function for this type of mixed effects model has been derived in detail by Tward et al.[89] Below we summarize the equations to solve for α, σ^2, ρ^2, and log-likelihood $l(\theta)$ given θ (Eqn 3.5, 3.6, and 3.7). Note that $|\cdot|$ denotes a matrix determinant, I_N is an $N \times N$ identity matrix, and constants independent of θ have been removed from the log-likelihood function:

$$\alpha = \left(X^T (I_N - B(B^T B + \frac{1}{\theta})^{-1} B^T) X\right)^{-1} \left(X^T (I_N - B(B^T B + \frac{1}{\theta})^{-1} B^T) Y\right), \tag{3.5}$$

$$\begin{aligned} \sigma^2 &= \frac{1}{N} (Y - X\alpha)^T (I_N - B(B^T B + \frac{1}{\theta})^{-1} B^T)(Y - X\alpha), \\ \rho^2 &= \theta\sigma^2, \end{aligned} \tag{3.6}$$

$$
\begin{aligned}
l(\theta) = &- \frac{N}{2}\log\left((Y - X\alpha)^T(I_N - B(B^TB + \frac{1}{\theta})^{-1}B^T)(Y - X\alpha)\right) \\
&+ \frac{1}{2}\log|I_N - B(B^TB + \frac{1}{\theta})^{-1}B^T|.
\end{aligned} \tag{3.7}
$$

We can then conduct a hypothesis test using $10,000$ bootstrap samples. We then follow up with a pairwise post-hoc testing between groups and a Bonferroni correction for the number of group pairs tested. The distributions of maximum test statistics used in pair-wise tests are calculated using the entire set of vertices. The vertices tested in the post-hoc test are limited to vertices significant in the original test.

Let us now step through pairwise post-hoc testing in our specific example. We modify the null hypothesis to test whether there is a difference between stable NC and NC to MCI converters. Eqn 3.8 corresponds to the null hypothesis and Eqn 3.2 corresponds to the alternate hypothesis:

$$
\begin{aligned}
\log(\text{thickness})_{i,j,k} = &a_k + b_k\ \text{age}_{i,j} \\
&+ \left(a''_k + b''_k(\text{age}_{i,j} - \text{age\_DEMonset}_i)\right)\text{isMCI}_i \\
&+ c_k\ \text{sex}_i + e_{i,k} + \epsilon_{i,j,k}.
\end{aligned} \tag{3.8}
$$

Next, we modify the null hypothesis to test for a difference in cortical thickness between stable NC and MCI to DEM converters. Eqn 3.9 corresponds to the null

hypothesis and Eqn 3.2 corresponds to the alternate hypothesis:

$$\begin{aligned}\log(\text{thickness})_{i,j,k} =& a_k + b_k\ \text{age}_{i,j} \\ &+ \left(a'_k + b'_k(\text{age}_{i,j} - \text{age\_MCIonset}_i)\right) \text{isPRE}_i \\ &+ c_k\ \text{sex}_i + e_{i,k} + \epsilon_{i,j,k}.\end{aligned} \tag{3.9}$$

Finally, we modify the null hypothesis to test for a difference in cortical thickness between NC to MCI converters and MCI to DEM converters. Eqn 3.10 corresponds to the null hypothesis and Eqn 3.2 corresponds to the alternate hypothesis:

$$\begin{aligned}\log(\text{thickness})_{i,j,k} =& a_k + b_k\ \text{age}_{i,j} \\ &+ \left(a'_k + b'_k(\text{age}_{i,j} - \text{age\_MCIonset}_i)\right) \text{isPRE}_i \\ &+ \left(a'_k + b'_k(\text{age}_{i,j} - \text{age\_DEMonset}_i)\right) \text{isMCI}_i \\ &+ c_k\ \text{sex}_i + e_{i,k} + \epsilon_{i,j,k}.\end{aligned} \tag{3.10}$$

At vertex locations where the alternative model significantly outperformed the null model, we can then calculate the difference in atrophy and atrophy rate. Atrophy rate (% per year) can be approximated as $100 * b$. This approximation holds true for relatively small values.

3.3 Experimental results

Using the method described in Section 3.2, we examined 69 subjects. The demographics of these subjects are shown in Table 3.1. There were no significant differences in age, sex, number of scans, or scan period stratified by diagnostic group. Note that the clinical follow-up period is longer than the scan period because scans that were introduced with a new scan protocol in ADNI3 were excluded from this analysis. Differences in scan protocol can introduce a source of bias, and while strategies have been developed for harmonizing cortical thickness across scanners, time-dependent harmonization is still an exploratory field.[90]

Diagnostic group	stable NC	NC to MCI	MCI to DEM
Sample size (n)	33	17	19
Baseline Age (years)	72.3 ± 5.5	74.9 ± 5.3	72.7 ± 6.4
Sex (% Female)	45.5	70.6	63.2
# of scans (years)	4.5 ± 0.6	4.6 ± 1.1	4.1 ± 0.8
Scan period (years)	3.4 ± 1.1	2.9 ± 1.0	2.0 ± 0.8
Clinical evaluation period (years)	5.3 ± 2.4	6.4 ± 3.7	4.1 ± 1.7

Table 3.1: Demographics (mean ± standard deviation where applicable)

We rejected the null hypothesis with a global $p < 0.0001$ and concluded that there was a difference in cortical thickness by diagnostic group. More specifically, we rejected the null hypothesis at 90% of vertices. Figure 3.1 shows the location and magnitude of disease-related atrophy compared to subjects with stable NC.

Using pairwise post-hoc testing, we rejected the null hypothesis for all three pairs of diagnostic groups (global $p < .0001$ for stable NC versus NC to MCI converters,

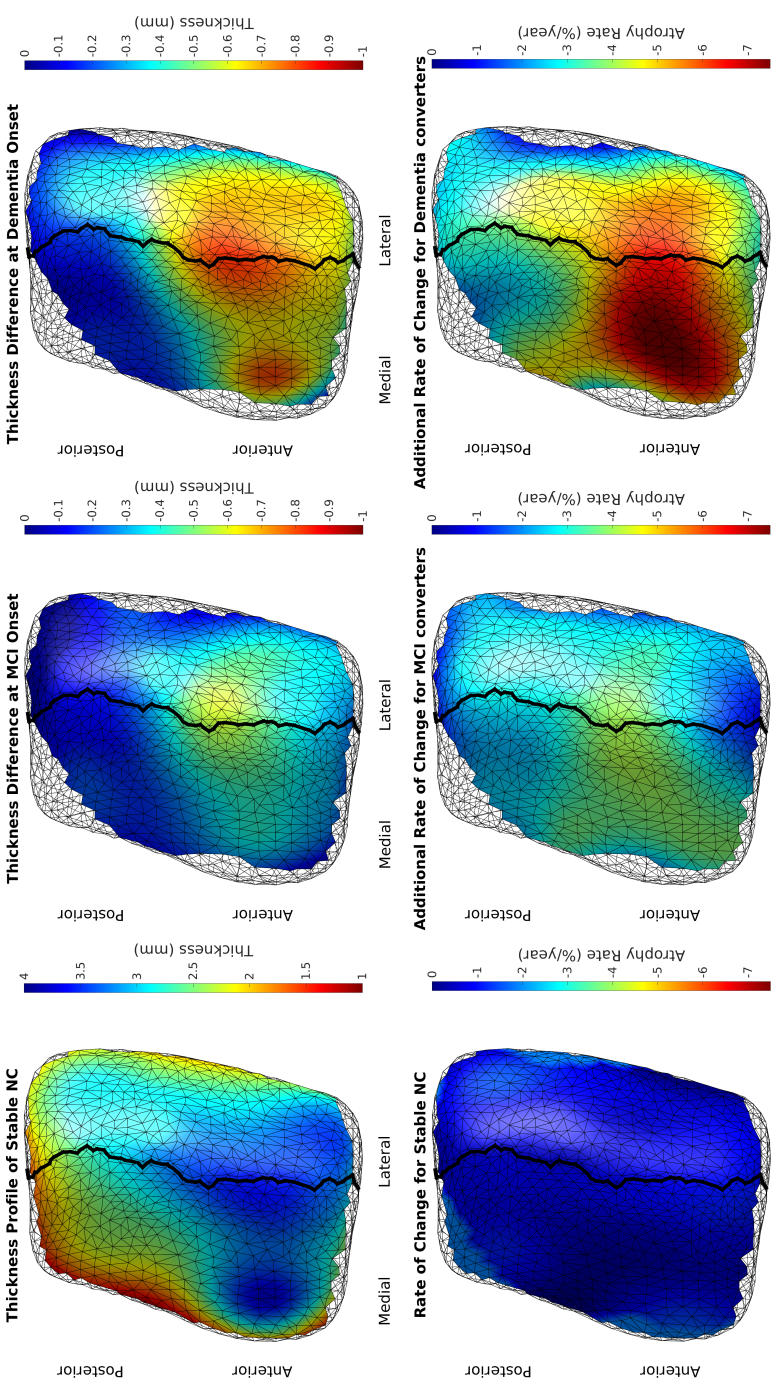

Figure 3.1: Results of group-wise difference analysis. Top left is the thickness profile of a stable NC at age 65, bottom left is the age-related atrophy rate. Top middle is the difference in thickness between stable NC and NC to MCI converters at the time of MCI diagnosis, and bottom middle is the additional disease-related atrophy in these subjects. Top right is the difference in thickness between stable NC and MCI to DEM converters at the time of DEM diagnosis, and bottom right is the additional disease-related atrophy in these subjects.

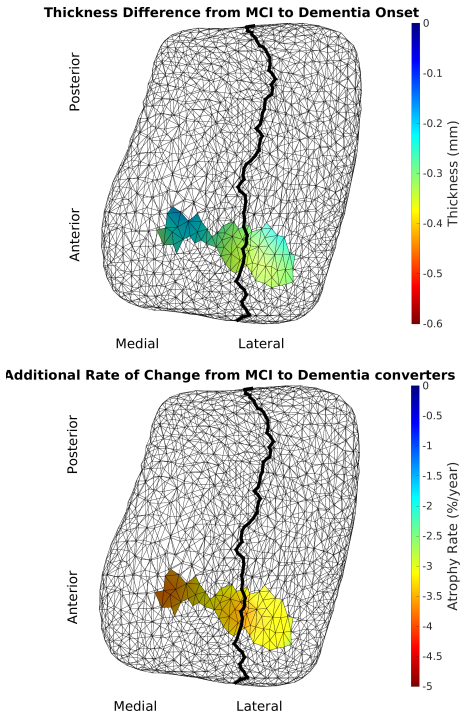

Figure 3.2: Results of pairwise post-hoc testing between NC to MCI converters and MCI to DEM converters. Top is the thickness difference from MCI diagnosis to DEM diagnosis, and bottom is the atrophy rate difference between these groups. Pair-wise results for the diagnostic groups compared to stable NC are not shown because all vertices tested rejected the null hypothesis, rendering regions identical to that displayed in Figure 3.1.

global $p < .0001$ for stable NC versus MCI to DEM converters, and global $p = .0002$ for NC to MCI converters versus MCI to DEM converters). We rejected the null hypothesis for all 90% of vertices in comparisons to stable NC. Between NC to MCI converters and MCI to DEM converters, we rejected the null hypothesis for 16% of vertices. These vertices are localized to the anterior lateral ERC and anterior TEC as shown in Figure 3.2.

A summary of average and maximum atrophy/atrophy rates over the rhinal cortex

is shown in Table 3.2. Note that the average atrophy and atrophy rates shown in Table 3.2 are the averages across vertices where the null hypothesis was rejected in pairwise post-hoc tests. The maximum atrophy detected over the rhinal cortex was in the anterior TEC with 0.54mm at the time of MCI diagnosis in NC to MCI converters, and 0.76mm at the time of DEM diagnosis in MCI to DEM converters when compared to stable NC subjects. Averaged across vertices, the TEC (ERC) was 0.22mm (0.27mm) thinner at the time of MCI diagnosis. The TEC (ERC) was 0.42mm (0.41mm) thinner at the time of DEM diagnosis.

The additional disease-related atrophy rate in participants who progressed from NC to MCI was 2.45% (3.07%) per year averaged across the TEC (ERC). This is a notable increase from age-related atrophy, which, on average, was 0.68% (0.76%) per year in the TEC (ERC). In other words, the average atrophy rate for NC to MCI converters was 5 (5) times greater than stable NC subjects. The average additional disease-related atrophy rate in the participants who progressed from MCI to DEM was 3.71% (4.81%) per year in the TEC (ERC). The average atrophy rate for MCI to DEM converters was approximately 6 (7) times greater than stable NC subjects.

In the anterior region, where a difference was detected between NC to MCI converters and MCI to DEM converters, there was an average additional atrophy of 3.55% (3.26%) per year in the TEC (ERC). At the time of DEM diagnosis, there was up to 0.34mm (0.40mm) of additional thinning in the TEC (ERC).

The evidence suggests that a significant amount of atrophy occurs prior to a

	ERC Average*	ERC Max	TEC Average*	TEC Max
atrophy at MCI diagnosis (with respect to stable NC)	0.27 mm	0.53 mm	0.22 mm	0.54 mm
atrophy at DEM diagnosis (with respect to stable NC)	0.41 mm	0.76 mm	0.42 mm	0.76 mm
atrophy at DEM diagnosis (with respect to atrophy at MCI diagnosis)	0.24 mm	0.37 mm	0.27 mm	0.31 mm
age-related atrophy rate	0.76 %/year	1.97 %/year	0.68 %/year	1.47 %/year
MCI-related atrophy rate (with respect to age-related atrophy rate)	3.07 %/year	4.12 %/year	2.45 %/year	3.95 %/year
DEM-related atrophy rate (with respect to age-related atrophy rate)	4.81 %/year	7.66 %/year	3.71 %/year	6.46 %/year
DEM-related atrophy rate (with respect to MCI-related atrophy rate)	3.26 %/year	3.78 %/year	3.06 %/year	3.55 %/year

Table 3.2: Summary of group-wise difference analysis by region. *The average was calculated *over the region of vertices where the null hypothesis was rejected* in pairwise tests and not the whole region, for a subject at age 75 and with sex = 0.5.

diagnosis of MCI throughout the rhinal cortex, and that the largest changes are detected in the anterior region between the border of the TEC and ERC. There is also evidence that the rate of atrophy increases over the progression of this disease.

3.4 Change-point analysis

In this section, we outline the construction of change-point analysis using cortical thickness data and two diagnostic groups. The approach can be modified to use other shape metrics and to model diseases other than AD. Unlike group-wise difference analysis, where we modeled subjects as members of separate diagnostic groups, here we use change-point analysis to model subjects as being part of one disease continuum. This type of analysis cannot be used to compare multiple disease etiologies.

We are interested in determining when the earliest signs of atrophy related to AD begin using a piece-wise linear model. Following the example from Section 3.2, MCI to DEM converters are not included in this analysis since the atrophy rate in this later stage of AD is substantially larger than the atrophy rate in NC to MCI converters. This was shown in the experimental results of group-wise difference analysis in Section 3.3.

We can test for when a change-point occurs with respect to the age of MCI diagnosis. Given a subject i, scan j, and region k, the null hypothesis can be written as

Eqn (3.11):

$$\log(\text{thickness})_{i,j,k} = a_k + b_k \ \text{age}_{i,j} + c_k \ \text{sex}_i + d_k \ \text{age\_MCIonset}_i + e_{i,k} + \epsilon_{i,j,k}. \quad (3.11)$$

The constants a, b, c, and d, as well as the variance of zero-mean Gaussians e and ϵ are estimated by maximum likelihood. e represents a subject-specific random effect. Age and the binary indicator variable for sex are fixed effects. For this model, we examine the cortical thickness of only two locations, which reduces computational complexity. Specifically, we examine average ERC thickness, and average TEC thickness.

The model under the alternative hypothesis can be written as Eqn (3.12):

$$\begin{aligned}\log(\text{thickness})_{i,j,k} =& a_k + b_k \text{age}_{i,j} + b'_k(\text{age}_{i,j} - (\text{age\_MCIonset}_i + \Delta))^+ \\ &+ c_k \text{sex}_i + d_k \text{age\_MCIonset}_i + e_{i,k} + \epsilon_{i,j,k}.\end{aligned} \quad (3.12)$$

Again, the constants a, b, c, d, and the variance of zero-mean Gaussians e and ϵ are estimated by maximum likelihood. However, we introduce a new variable Δ, which represents the number of years between a diagnosis of MCI to a change in atrophy rate. Then, $(\text{age}_{i,j} - (\text{age\_MCIonset}_i + \Delta))^+ = \max(\text{age}_{i,j} - (\text{age\_MCIonset}_i + \Delta), 0)$ is the number of years a specific observation is past the change point. We perform maximum likelihood estimation for a fixed Δ, and increment Δ yearly between -50 and 50 to find the best change point candidate. The best candidate, Δ, is calculated

from the posterior mean.

For stable NC subjects, we estimate the age of MCI diagnosis from a conditional probability distribution. The age of onset is constrained to be after the last diagnostic evaluation, and is drawn from a Gaussian distribution with a mean of $\mu_1 = 93$ years old and a standard deviation of $\sigma_1 = 14.5$ years. This distribution of MCI diagnosis age was estimated by Tang et al[87] using a set of $1,000$ subjects enrolled with normal cognition and a family history of Alzheimer's disease. These diagnostic criteria are similar to the conditions under which subjects with stable NC were enrolled in the ADNI study. The bootstrapped samples are then constructed by sampling from whitened residuals under the null hypothesis, with imputed values of age_MCIonset for stable NC subjects.

One underlying assumption of this analysis is that the sample of subjects are selected from the disease continuum at random, and therefore represent the distribution of the disease course. This criteria is met when subjects are enrolled without any selection based on disease stage, or when relatively younger subjects are selected with NC at the time of enrollment and followed for an extensive period of time. However, it is often the case that data sets are acquired with a selection process dependent on the disease stage, as with the ADNI study. In order to address this added complexity, we used the following approach.

We can re-weight the likelihood function using a distribution of stable NC and NC to MCI converters expected if the subjects had been selected blind to their di-

agnostic stage. We examined the BIOCARD database, where subjects were enrolled cognitively normal and followed for up to 22 years at time examined (biocard-se.org). The distribution is calculated from a subset of subjects over the age of 65 at their most recent diagnostic follow-up.

The log-likelihood function associated with these models have been derived in detail by Younes et al.[88] By iterating over fixed change-points Δ instead of incorporating Δ as a variable to perform maximum likelihood estimation over, we simplify the model to a linear mixed effects model (recall that the effect of Δ as a variable is non-linear). We perform gradient descent with MATLAB's function fmincon by supplying the gradient with respect a, b, b', c, d, ρ, and σ. Supplying the gradient speeds up the computation time, which is important for computationally-heavy resampling procedures.

In the case that the null hypothesis is rejected, we can follow up by calculating confidence intervals for the variables of interest. These variables are: $-\Delta$, the change point with respect to MCI diagnosis time; $-b$, the age-related atrophy rate; $-b'$, the disease-related additional atrophy rate after the change point. Note, again, that the samples are constructed with imputed values of age_MCIonset for stable NC subjects.

In the case that the null hypothesis is rejected for both ERC and TEC, we can pose a follow-up hypothesis. This hypothesis is based on the histological changes, which occurs in the TEC prior to the ERC. We can calculate the probability that the change point occurred in the TEC prior to the ERC based on the change point Δ of

	Change point (years before MCI)	Age-related rate (%/year atrophy)	Disease-related rate (%/year atrophy)
ERC thickness	(7.63, 11.31)	(0.07, 0.65)	(3.03, 4.41)
TEC thickness	(8.92, 13.80)	(0.10, 0.56)	(2.11, 3.08)

Table 3.3: 95% confidence interval (min, max). Change point, age-related rate, and disease-related rate correspond to the variables $-\Delta$, $-b$, and $-b'$ respectively. The disease-related rate is the additional rate seen post change point. this table is reproduced with permission.[70]

each pair of bootstrapped samples under the alternative hypothesis.

3.5 Experimental results

Using the method described in Section 3.4, we examined 50 subjects. These demographics of these subjects were previously described in Table 3.1. Figure 3.3 shows the input into the model, which is average cortical thickness over the TEC and ERC, respectively. Qualitatively, it is clear from this figure that the atrophy rate for stable NC is smaller in magnitude than NC to MCI converters in both regions of interest.

We rejected the null hypothesis and conclude that there was a change point 10.69 years prior to an MCI diagnosis in the TEC ($p < 0.001$), and 9.02 years prior to an MCI diagnosis in the ERC ($p < 0.001$). The age-related atrophy rate (or atrophy rate prior to the change-point) was 0.34% per year (0.35% per year) in the TEC (ERC).

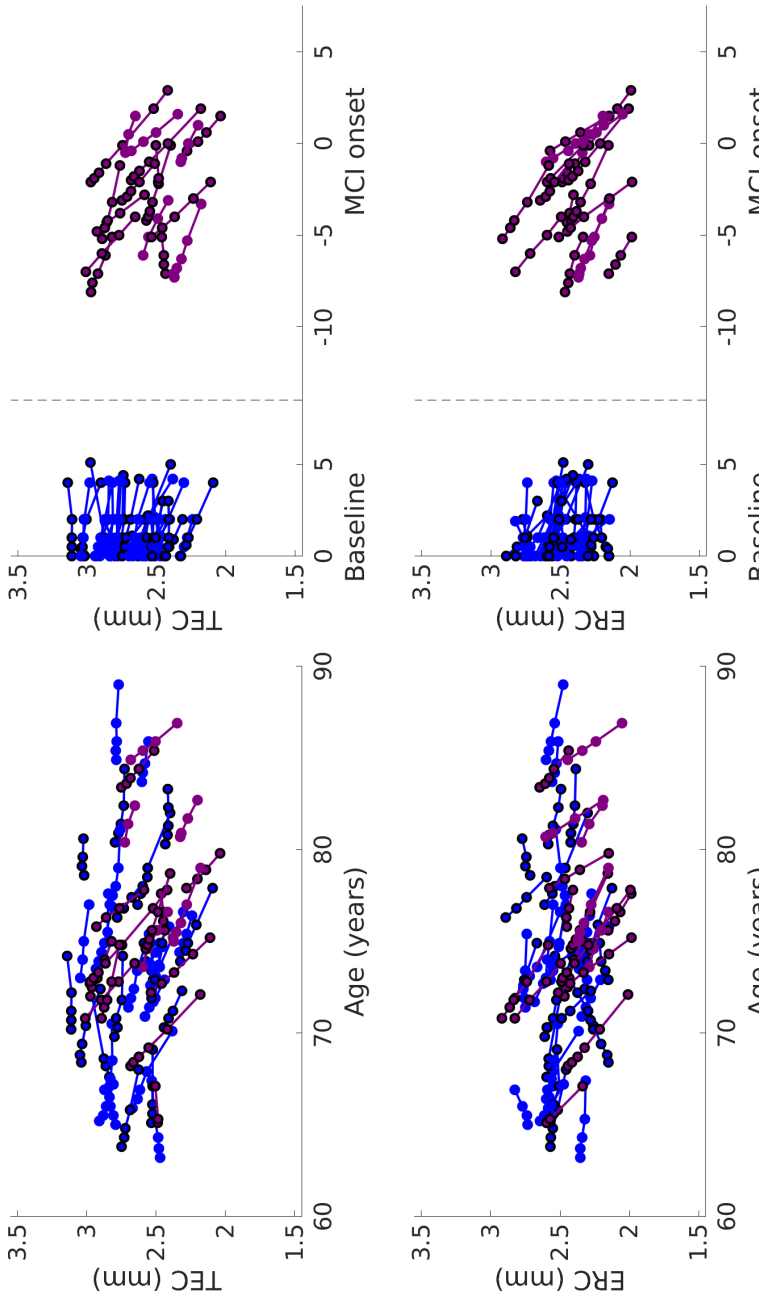

Figure 3.3: Average cortical thickness over the TEC (top) and ERC (bottom). The left figures are organized by age, whereas the right figures are organized by scan date for stable NC and conversion date for NC to MCI converters. Each line corresponds to a subject, the color to a diagnostic group (stable NC, NC to MCI), and the marker border to sex (no border is male, bordered is female). This figure is reproduced with permission.[70]

After the change point, the additional disease-related atrophy introduced was 2.58% per year in the TEC and 3.75% per year in the ERC. On average, the ERC was slightly thinner and the percentage atrophy rates are slightly larger than in the TEC.

We next calculated a confidence interval for the atrophy rates and change-points. The 95% confidence interval for the parameters of interest are shown in Table 3.3. The change-point is estimated with a confidence interval of approximately 4 years. The ERC change point occurred at or before the TEC change point only in 3.75% of bootstrapped samples. Therefore, we conclude that the change-point for the TEC precedes the ERC. This statement agrees with the pattern of early AD-related NFT accumulation in the rhinal cortex. These findings suggest that irreversible neuron death is detected in the rhinal cortex at least 9 years prior to an official diagnosis of cognitive impairment. By increasing the sensitivity of AD detection during this preclinical stage, there will be a larger window of opportunity for disease-modifying treatments.

3.6 Summary

In this chapter, we have introduced a statistical framework that can be used in conjunction with the morphological pipeline introduced in Chapter 2. These methods can be used to determine where and when disease-related atrophy occurs, which is important for improving the sensitivity and specificity of early AD detection. Boot-

strap resampling the maximum test statistic over a set of vertices allows us to conduct hypothesis tests and build confidence intervals while controlling the family-wise error rate. The experimental results for early AD data show several biologically significant results. The major results are summarized below.

Using group-wise difference analysis, we showed that the anterior regions of the TEC and ERC were 0.58mm thinner at the time of MCI diagnosis and 0.83mm thinner at the time of DEM diagnosis. Given that the anterior rhinal cortex is between 3 and 4mm thick, this suggests a substantial amount of grey matter has atrophied prior to any clinical diagnosis.

Age-related atrophy was less than 1% per year. By comparison, NC to MCI converters experienced an additional 2 to 3% disease-related atrophy per year; MCI to DEM converters experienced an additional 4 to 5% disease-related atrophy per year. There was a significant difference in atrophy rate between the NC to MCI converters and MCI to DEM converters, suggesting that the rate of atrophy increases over the progression of this disease.

Using change-point analysis, we showed that disease-related atrophy begins in the TEC prior to the ERC, mimicking the pattern of neurofibrillary tau accumulation seen in autopsy reports.[91] The change-point occurred 9 to 14 years prior to MCI diagnosis in the TEC, and 8 to 11 years prior to MCI diagnosis in the ERC. This suggests there is a long window of opportunity to stage the disease and intervene prior to the onset of symptoms.

Chapter 4

Subject-specific analysis

We now develop a subject-specific mechanistic model of atrophy spread in the rhinal cortex. We start by introducing the biological motivation for a reaction-diffusion model. We propose a continuous model concept, then discuss the details of a discrete numerical implementation. Next, we derive an approach to estimate model parameters using an adjoint state method for gradient descent. We test the model accuracy on a simulation of AD progression, and then show results on real subject data. The overarching aim is to locate the initial source of disease, the speed of disease spread, and other disease parameters that are estimated from an individual's MRIs over time. This type of patient-specific modeling is still in its infancy and, as seen in other patient-specific models, we focus on model feasibility and proof-of-concept with a small number of subjects.[92,93] This chapter has been modified in part from a relevant publication.[77]

4.1 Biological Motivation for Model

There is an established body of evidence that NFT accumulation is spatially-temporally ordered. Accumulation begins in the TEC and progresses to the ERC and CA1 region of the hippocampus, then to the rest of the hippocampus and parts of the amygdala, and finally spreads into the neocortex.[12–14,16,18,23,91] Change-point analysis of atrophy as measured from structural MRI also support spatial-temporal ordering. 9 - 14 years prior to cognitive impairment, the first changes are seen in the TEC, quickly followed by the ERC, and then later in the hippocampus and amygdala.[70,88]

NFT accumulation and atrophy patterns are also in line with what is understood about the structural and functional connectivity of this region. Specifically, the TEC is a major contributor of input to the anterior lateral ERC,[72,81] a secondary contributor of input to the anterior proximal subiculum bordering CA1,[72,94] and also a contributor to the basolateral and basomedial nuclei of the amygdala.[95]

Recently, a prion-like propagation hypothesis of neurodegenerative disease spread has gained traction.[96–101] There is evidence that misfolded tau proteins aggregate and further seed conversion of normal tau to misfolded tau.[24,98,102] Then, it is believed that these misfolded tau aggregates propagate by cell release, diffusion, and cell uptake along axonal pathways.[98] Recent PET studies show a strong regional association of tau tracer retention that progresses in a Braak-stage like pattern.[103–105]

Multipolar reelin-positive neurons found in Layer II of the TEC and ERC, also

referred to as pre-α neurons, are the primary target of NFT accumulation during Braak stages I to III.[12,106] In rodents and primates, it has been shown that these neurons are connected by a microcircuit of interneurons that are confined within the layer.[106,107] In particular, Layer II grid cells of the medial ERC have been studied extensively, and it has been shown that interneurons connect and inhibit *neighboring* principal neurons.[106] We hypothesize that connectivity within the rhinal cortex can be modeled as a function of distance. The spatio-temporal pattern of atrophy, prion-like propagation hypothesis, and regional connectivity motivate modeling cortical atrophy across the rhinal cortex as a reaction-diffusion process.

4.2 Continuous formulation

The goal is to model cortical thickness atrophy as a function of disease. Let us consider a model where cortical thickness is a sigmoidal function of disease stage, as shown in Figure 4.1. There is some age-related atrophy, and so total atrophy intensifies as the disease stage increases and introduces disease-related atrophy over time. The disease stage, in turn, progresses as a reaction-diffusion function of local activity, which is loosely based on NFT accumulation.

We now specify the model in more concrete terms. We start by introducing variable s to represent a location in the spatial domain Ω, and t represent a time in the temporal domain $[t_0, t_1]$. Cortical thickness, $\rho(s,t)$, is defined to be a sigmoidal

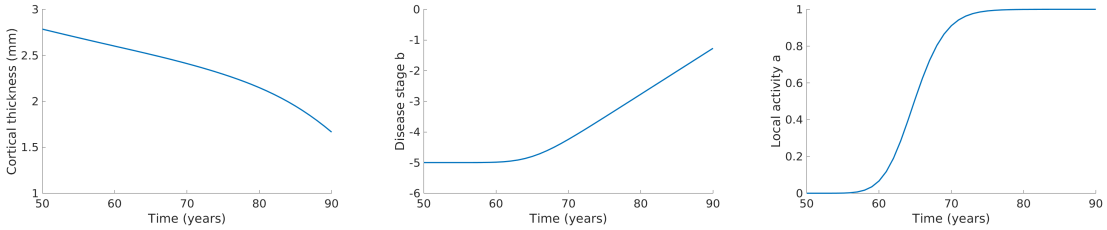

Figure 4.1: Cortical thickness as a function of time (left), disease stage as a function of time (middle), and local activity as a function of time (right). This figure has been reproduced with permission.[77]

function of the stage of the disease, $b(s,t)$, and aging, $\lambda_0 t$. This is shown in Eqn 4.1. The disease stage, $b(s,t) \in (-\infty, \infty)$, grows larger as the disease progresses and is closely linked to disease-related atrophy. Note that the smaller b^0 is, the longer it takes a subject to display disease-related cortical thinning, with all other variables held constant. In this sense, b^0 can also be thought of as a susceptibility measure to the disease.

The rate of disease progression, $\partial_t b(s,t)$, is controlled by the disease intensity, $\lambda_1 > 0$, and local activity rate, $a(s,t)$, as shown in Eqn 4.2. This local activity rate, $a(s,t) \in [0,1]$, is loosely based on the environmental conditions needed to support disease progression, such as the concentration of NFT. We model $a(s,t)$ as a Fisher-KPP equation with a diffusion rate of D and a reaction rate of κ, as shown in Eqn 4.3. To understand how a functions, we examine its fixed points. There is an unstable fixed point $a(s,t_0) = 0$ for all s, from which the disease cannot progress. However, when $a(s_0,t_0)$ is seeded with a non-zero value at any location, we end up at a stable fixed point of $a(s,t_1) = 1$ for all s. As a final note, we impose a Neumann boundary

condition on the local activity rate $a(s,t)$ since the surface is open:

$$\rho(s,t) \quad = \rho_{\max}(s)\frac{e^{-\lambda_0(s)t}}{1+e^{b(s,t)}}, \tag{4.1}$$

$$\partial_t b(s,t) = \lambda_1 a(s,t), \tag{4.2}$$

$$\partial_t a(s,t) = D\Delta a(s,t) + \kappa a(s,t)(1-a(s,t)). \tag{4.3}$$

4.3 Discrete implementation

In order to find a numerical solution to the problem, we derive a discrete implementation of the model. Let us first introduce a new piece-wise continuous function, $\phi(s)$, and introduce a variational formulation of Eqn 4.3, as shown in Eqn 4.4:

$$\begin{aligned}\int_\Omega \partial_t a(s,t)\phi(s)ds \;-\; D\int_\Omega \langle\nabla a(s,t),\nabla\phi(s)\rangle ds \\ -\;\kappa\int_\Omega a(s,t)(1-a(s,t))\phi(s)ds \;=\; 0.\end{aligned} \tag{4.4}$$

Now we let $k \in 0,1,\ldots,K$ be indices of the discretized space, and more specifically, the indices of a triangulated mesh. Let $\phi_k(s)$ be a tent function with a constant gradient $\nabla\phi_k(s) = \nabla\phi_k$, defined for all s on a triangular face of the mesh. Using

a Galerkin approximation, we can represent local activity rate $a(s,t)$ as a sum of spatially discrete, temporally continuous $a_k(t)$, as shown in Eqn 4.5:

$$a(s,t) = \sum_{k=1}^{K} a_k(t)\phi_k(s). \tag{4.5}$$

We are now ready to introduce some notation commonly used in finite element methods: the mass matrix M, stiffness matrix S, and, in this model, a nonlinear reaction term F. Using Eqn 4.4 and Eqn 4.5, we write a set of equations as shown in 4.6:

$$\begin{aligned}
&M\partial_t a(t) + DSa(t) - \kappa F(a(t)) = 0,\\
&a(t) \quad = \begin{bmatrix} a_1(t) \\ \vdots \\ a_K(t) \end{bmatrix},\\
&M(k,k') = \int_\Omega \phi_k(s)\phi_{k'}(s)ds,\\
&S(k,k') \;= \int_\Omega \langle \nabla\phi_k(s), \nabla\phi_{k'}(s)\rangle ds,\\
&F(k) \quad = \int_\Omega \left(\sum_{k'=1}^{K} a_{k'}(t)\phi_{k'}(s)\right)\left(1 - \sum_{k'=1}^{K} a_{k'}(t)\phi_{k'}(s)\right)\phi_k(s)ds.
\end{aligned} \tag{4.6}$$

The following excerpt describes details on the implementation of M, S, and F:[77]

> "Computing M, S, and F as shown in [Eqn 4.6] is computationally intensive. Instead, we calculate an approximation using the properties of ϕ. Let $R = \{r_u, r_v, r_w\}$ be the set of 2-D vertices of a triangle. Let r_{uv} be the

midpoint of vertex r_u and r_v, and r_{uvw} be the barycenter of the triangle. The area of the triangle is then [Eqn 4.7]:

$$\text{area}(R) = \text{abs}\left(\frac{1}{2}\det\begin{vmatrix} 1 & 1 & 1 \\ r_u & r_v & r_w \end{vmatrix}\right). \tag{4.7}$$

We now can introduce 1st , 2nd and 3rd order approximations of $\phi(s)$ over a triangle in [Eqn 4.8], [Eqn 4.9], and [Eqn 4.10] respectively:

$$\int_R \phi(s)ds \approx \text{area}(R)\phi(r_{uvw}), \tag{4.8}$$

$$\int_R \phi(s)ds \approx \frac{\text{area}(R)}{3}\sum_{r_u,r_v\in R}\phi(r_{uv}), \tag{4.9}$$

$$\int_R \phi(s)ds \approx \frac{\text{area}(R)}{60}(3\sum_{r_u\in R}\phi(r_u) + 8\sum_{r_u,r_v\in R}\phi(r_{uv}) + 27\phi(r_{uvw})). \tag{4.10}$$

ϕ is a 1st order piece-wise linear function. Specifically, note that $\phi_k(r_k) = 1$, $\phi_k(r_{kv}) = \frac{1}{2}$ and $\phi_k(r_{kvw}) = \frac{1}{3}$. M can be represented as a 2nd order function, S can be represented as a 1st order function, and F can be represented as a 3rd order function summed over all the triangles R as shown in [Eqn 4.11], [Eqn 4.12], and [Eqn 4.13] respectively:

$$M(k,k') = \sum_{r_k,r_{k'}\in R}\frac{\text{area}(R)}{12}(1 + I_{k=k'}), \tag{4.11}$$

$$S(k,k') = \sum_{r_k,r_{k'}\in R}\text{area}(R)\langle\nabla\phi_k(r_{uvw}), \nabla\phi_{k'}(r_{uvw})\rangle, \tag{4.12}$$

$$F(k) = \sum_{r_k\in R}\frac{\text{area}(R)}{60}\Big(10a_{r_k} + 5a_{r_v} + 5a_{r_w} - 6(a_{r_k})^2 - 2(a_{r_v})^2 - 2(a_{r_w})^2 - 4a_{r_k}a_{r_v} - 4a_{r_k}a_{r_w} - 2a_{r_v}a_{r_w}\Big)." \tag{4.13}$$

This completes the approach for discretizing Eqn 4.6 with respect to space. We now turn our attention to discretizing the equation with respect to time and introduce indices $n \in 0, 1, \ldots, N$ of discretized time t_n. We fix the step size to be Δt and

introduce notation $a^n = a(t_n)$. We discretize Eqn 4.6 using a semi-implicit scheme, which results in Eqn 4.14. While the semi-implicit scheme is more complicated to implement than an explicit scheme, the semi-implicit scheme is preferred because it provides error bounds and a numerically stable solution. The final set of equations discretized in space and time are shown in Eqn 4.15, with M, S and F defined from Eqn 4.11, 4.12 and 4.13, respectively:

$$M(a^{n+1} - a^n) + \Delta t D S a^{n+1} - \Delta t \kappa F(a^n) = 0, \tag{4.14}$$

$$\begin{aligned} a^{n+1} &= (M + \Delta t D S)^{-1}(M a^n + \Delta t \kappa F(a^n)) \\ b^{n+1} &= b^n + \lambda_1 \Delta t a^n \\ \hat{\rho}^{n+1} &= \rho_{\max} \circ \frac{e^{\lambda_0 \Delta t (n+1)}}{1 + e^{b^{n+1}}}. \end{aligned} \tag{4.15}$$

4.4 Model simplifications

We now modify the model in order to reduce the number of dimensions to represent the parameter space. This is to make the parameter estimation problem tractable. We constrain the initial local activity rate, a^0, to be a Gaussian distribution centered about c^0, with fixed variance $\sigma^2 = 1$ in all directions. This simplification is shown in Eqn 4.16 with d equal to the number of dimensions of c^0. Next, the initial disease

stage, b^0, is constrained to be constant $\bar{b}^0$ throughout the surface:

$$a^0(x) = \frac{1}{(2\pi\sigma^2)^{d/2}} \exp\left(-(x-c^0)^T \frac{1}{2\sigma^2}(x-c^0)\right). \tag{4.16}$$

Age-related atrophy rate, λ_0, and cortical thickness prior to any changes, $\rho_{\max}$, cannot be simplified to a constant; there is variation in thickness and atrophy rate over the surface that is necessary to capture. Instead, we use a model beforehand with a separate data set to estimate variation in thickness over space, h, and age-related atrophy rate, λ_0.

Specifically, we use the mixed effects model shown in Eqn 4.17 to estimate the spatial variation in thickness, the effects of age and sex, and the variance of Gaussian noise ϵ. This is a model of cortical thickness (thk) for a *healthy* subject i, at scan j, and at vertex k:

$$\begin{aligned} \log(\text{thk})_{i,j,k} &= \mu_i + \text{shape}(k) - \lambda_0(k)\ t_{i,j} + \delta(k)\ \text{sex}_i + \epsilon_{i,j,k}, \\ h(k) &= e^{\text{shape}(k)}. \end{aligned} \tag{4.17}$$

λ_0 and h are estimated per vertex from the model and then held fixed in the atrophy spread model. The resulting $\rho_{\max}$ is then a function of a 1-dimensional

average cortical thickness $\bar{\rho}_{\max}$, as shown in Eqn 4.18:

$$\rho_{\max}(k) = \bar{\rho}_{\max}\ h(k). \tag{4.18}$$

The simplified model parameters, θ, are shown in Equation 4.19. We have reduced the number of dimensions from $4K+3$ to 7, where K is the total number of vertices:

$$\theta^T = \begin{bmatrix} \kappa & D & \lambda_1 & \bar{\rho}_{\max} & c^0 & \bar{b}^0 \end{bmatrix}. \tag{4.19}$$

To wrap up this section, we introduce some new notation, shown in Eqn 4.20, and write the atrophy spread model in simplified terms, as shown in Eqn 4.21:

$$x = \begin{bmatrix} x^1 \\ \vdots \\ x^N \end{bmatrix}, \quad x^n = \begin{bmatrix} x_1^n \\ \vdots \\ x_K^n \end{bmatrix}, \quad x_k^n = \begin{bmatrix} a_k^n \\ \\ b_k^n \end{bmatrix}, \tag{4.20}$$

$$\begin{aligned} f_n(x^n, \theta) &= \begin{bmatrix} (M + \Delta t D S)^{-1}(Ma^n + \Delta t \kappa F(a^n)) \\ \\ b^n + \lambda_1 \Delta t a^n \end{bmatrix} - x^{n+1}, \\ f(x, \theta) \quad &= \begin{bmatrix} f_n(x^0, \theta) \\ \vdots \\ f_n(x^{N-1}, \theta) \end{bmatrix} = \mathbf{0}_{2MN \times 1}. \end{aligned} \tag{4.21}$$

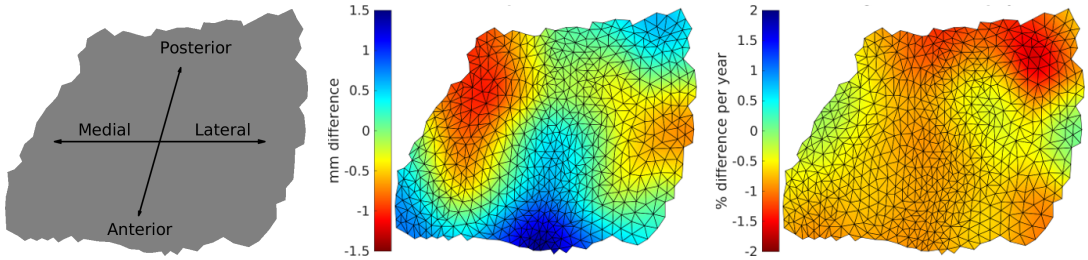

Figure 4.2: On the left is orientation across the surface, in the middle is vertex-wise difference in shape, and on the right is age-related change over time. This figure has been modified and reproduced with permission.[77]

4.5 Simulation generation

We generate a simulation of AD-related atrophy using the atrophy spread model with model simplifications. First, a set of 15 subjects with stable NC were fed into the mixed effects a priori model to estimate λ_0, h, and $\bar{\rho}_{\max}$. Figure 4.2 shows the estimated shape and age-related change over time, or $-\lambda_0$.

As with the experimental results shown for population level analysis, the criteria for stable NC was a clinical dementia rating equal to 0 on all annual evaluations, evidence of performance within the normal range on the Logical Memory Subtest of the Wechsler Memory Scale on all annual evaluations, and a negative result for elevated amyloid β levels on the baseline evaluation (as established by the ADNI Biospecimen Core). Subjects were also scanned on a consistent type of 3T MRI for 2 or more years. As shown in Table 4.1, half the subjects were female, and had an average age of 71 at the time of the baseline scan. All subjects were between 60 and 90 years old.

Number of Subjects	15
Age (years)	71.44 ± 7.17
Number of Scans	4.53 ± 0.52
Scan Period (years)	3.36 ± 1.14
Follow-up Period (years)	5.67 ± 3.22
Sex (% Female)	46.67%

Table 4.1: Demographic data for stable NC subjects used to generate a priori estimates (mean $\pm$ standard). Note that the scan period is shorter than the follow-up period because accelerated 3T scans introduced in ADNI3 were excluded from analysis.

The rhinal cortex pipeline described in Chapter 2 was implemented to calculate vertex-wise measures of cortical thickness. The pial cut of the template surface is the surface used to generate the simulation of atrophy spread. The top row of Figure 4.3 shows the progression of age-related atrophy using the a priori model with this set of data.

To select the remaining parameters, (namely disease-related parameters c^0, b^0, λ_1, κ, and D), we incorporated what is currently understood about AD from literature. We initialize local activity, c^0, to begin in the anterior lateral region. Histological studies have shown neurofibrillary tangles first form in the lateral rhinal cortex,[12] and disease-related atrophy measured from MRI data further suggests that the initial location is anterior lateral rhinal cortex,[85].[70] We initialize disease stage, b^0, to -5 such that disease-related atrophy is less than 1% at age 50, when the model initializes. Subjects are typically diagnosed with cognitive impairments or probable AD dementia after the age of 65; in these cases, very little or no atrophy is expected at age 50.

The disease intensity, λ_1, is set to 0.09. This estimate is chosen based on a set

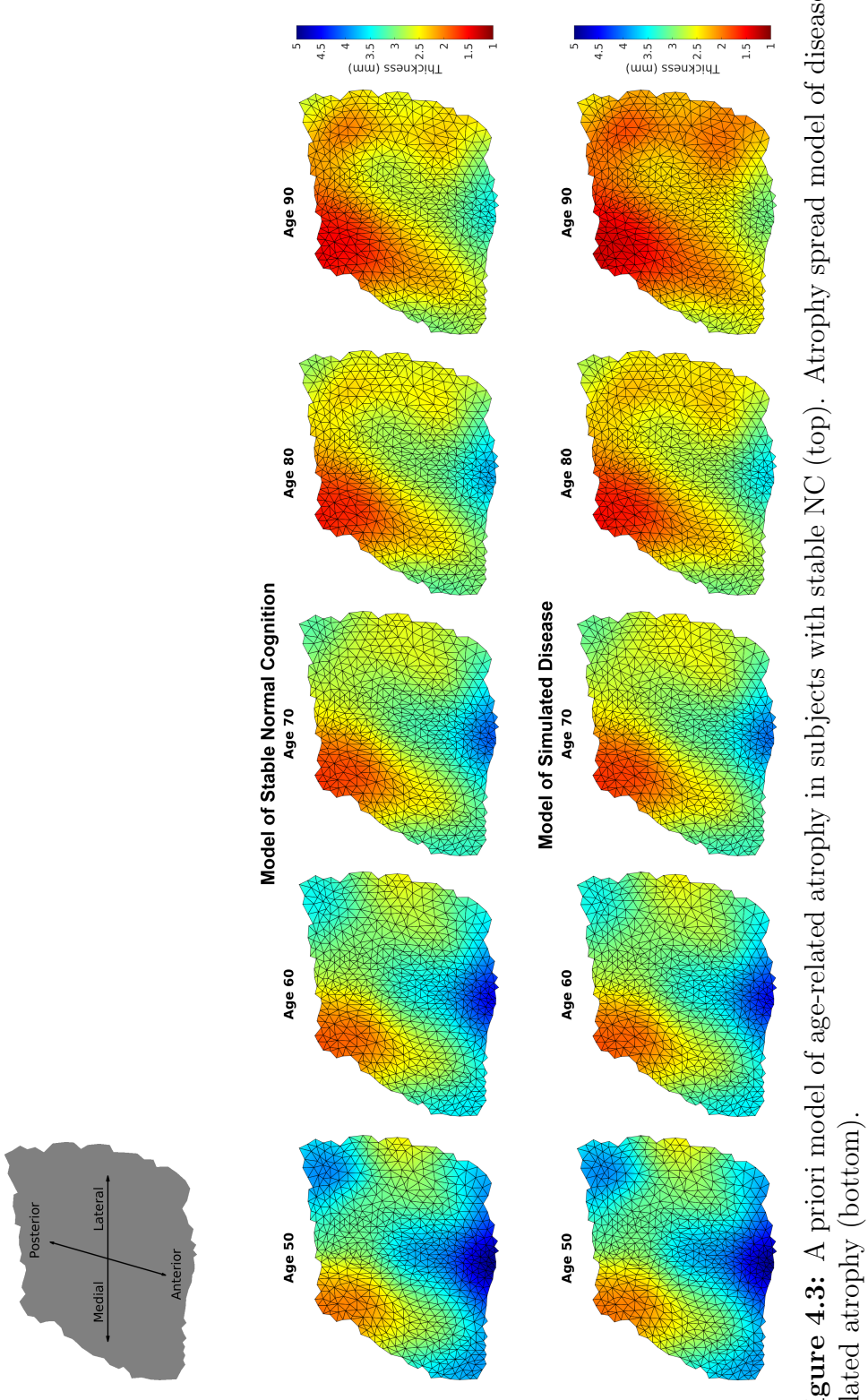

Figure 4.3: A priori model of age-related atrophy in subjects with stable NC (top). Atrophy spread model of disease-related atrophy (bottom).

of probable AD dementia data that was previously introduced in Section 2.6 and Section 3.3. The set of 19 dementia subjects showed 15.1% atrophy at the time of diagnosis compared to the set of 33 stable NC subjects. Additionally, these subjects experienced 4.05% disease-related atrophy per year. We then considered a simplified model where b is constant across the surface, with a time step $dt = 1$ year. We approximated $\lambda_1 = 0.09$ in the following way:

$$\begin{aligned}
\frac{1}{1+e^{b}} &= 1 - 0.151, \\
\frac{1}{1+e^{b+\lambda_1}} &= (1-0.151)(1-0.0405), \\
b &= \log(\frac{0.151}{1-0.151}) = -1.73, \\
\lambda_1 &= \log(\frac{1-(1-0.151)(1-0.0405)}{(1-0.151)(1-0.0405)e^{b}}) = 0.09.
\end{aligned}$$

Finally, we selected $\kappa = 1$ and $D = 1$. There is little data to estimate these parameters from. Note that $\sqrt{\kappa D}$ is the speed of spread across the surface, and $\sqrt{\frac{\kappa}{D}}$ is the slope of local activity rate a at the wave front. κ and D were chosen such that local activity rate a traverses the surface in 10 years with a slope of 1 $\frac{1}{\text{mm}}$.

In summary, the construction of AD simulation with the atrophy spread model

used the following parameters:

$$\kappa = 1.00, \quad c_x^0 = -6.00,$$

$$D = 1.00, \quad c_y^0 = -4.00,$$

$$\lambda_1 = 0.09, \quad b^0 = -5.00,$$

$$\bar{\rho}_{\max} = 3.38.$$

Figure 4.4 and 4.5 shows the local activity a, disease stage b, and cortical thickness ρ over the rhinal cortex from age 50 to 90 in this simulation. Notice that the disease is seeded to begin at age 50, and that the disease-related atrophy is very small compared to the natural variation in thickness across the surface of the rhinal cortex. This highlights the importance of capturing cortical thickness prior to age-related and disease-related effects accurately.

4.6 Parameter estimation

Given a set of cortical thickness observations over time, we solve for the optimal parameters θ that minimize the squared distance between observed and modeled cortical thickness. This is a constrained optimization problem with constraints $f(x, \theta) = 0$, as shown in Eqn 4.21 (reproduced below), and cost function $g(x, \theta)$, as shown in Eqn 4.22. $\hat{\rho}$ is the modeled cortical thickness that implicitly depends on x and θ, and ρ is

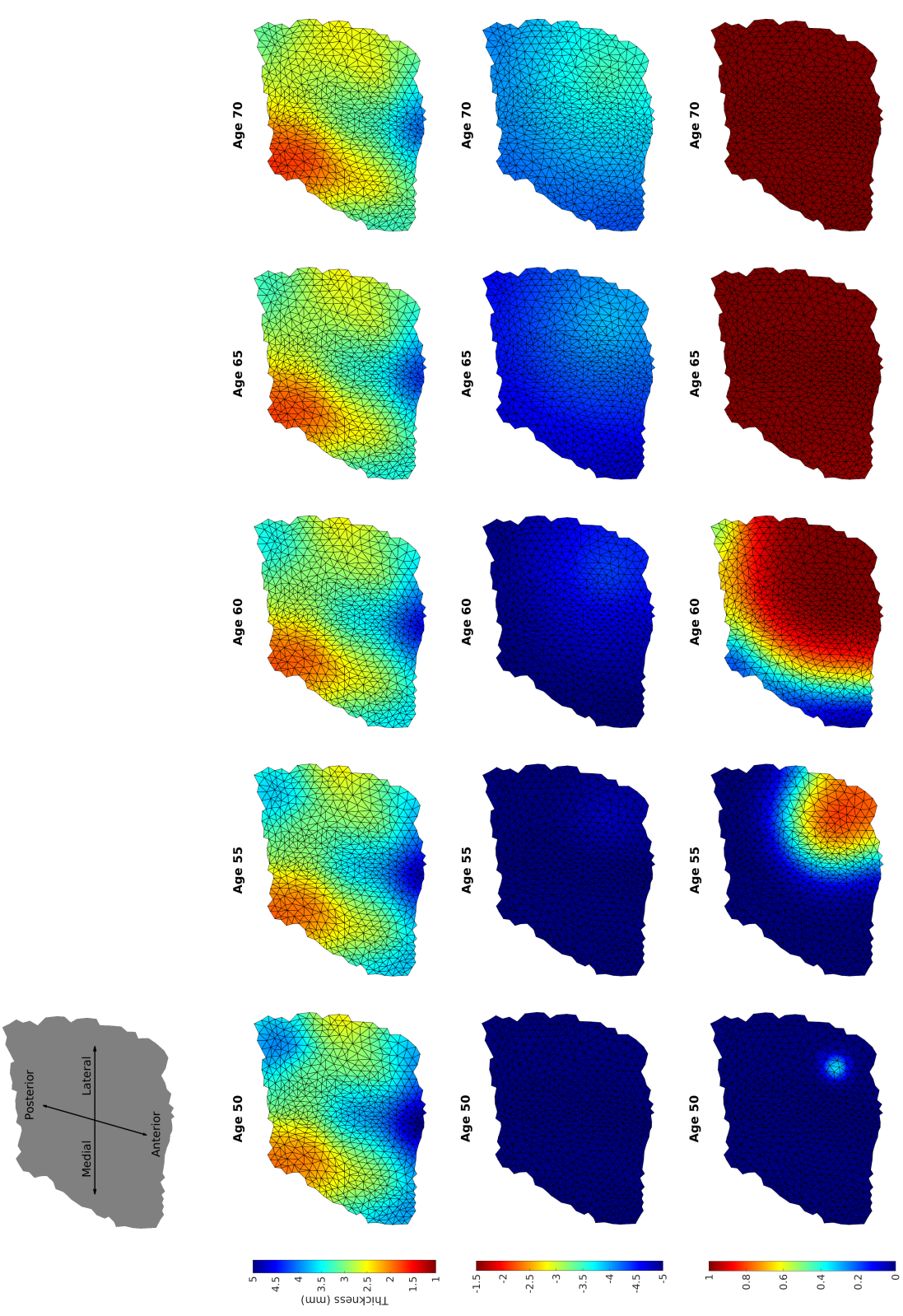

Figure 4.4: Simulation of AD using the model of atrophy spread. Cortical thickness (top), disease stage (middle), and local activity rate (bottom) over the rhinal cortex from age 50 to 70 in 5 year intervals. The surfaces are oriented such that left is medial, right is lateral, top is posterior, and bottom is anterior. Figure is reproduced with permission.[77]

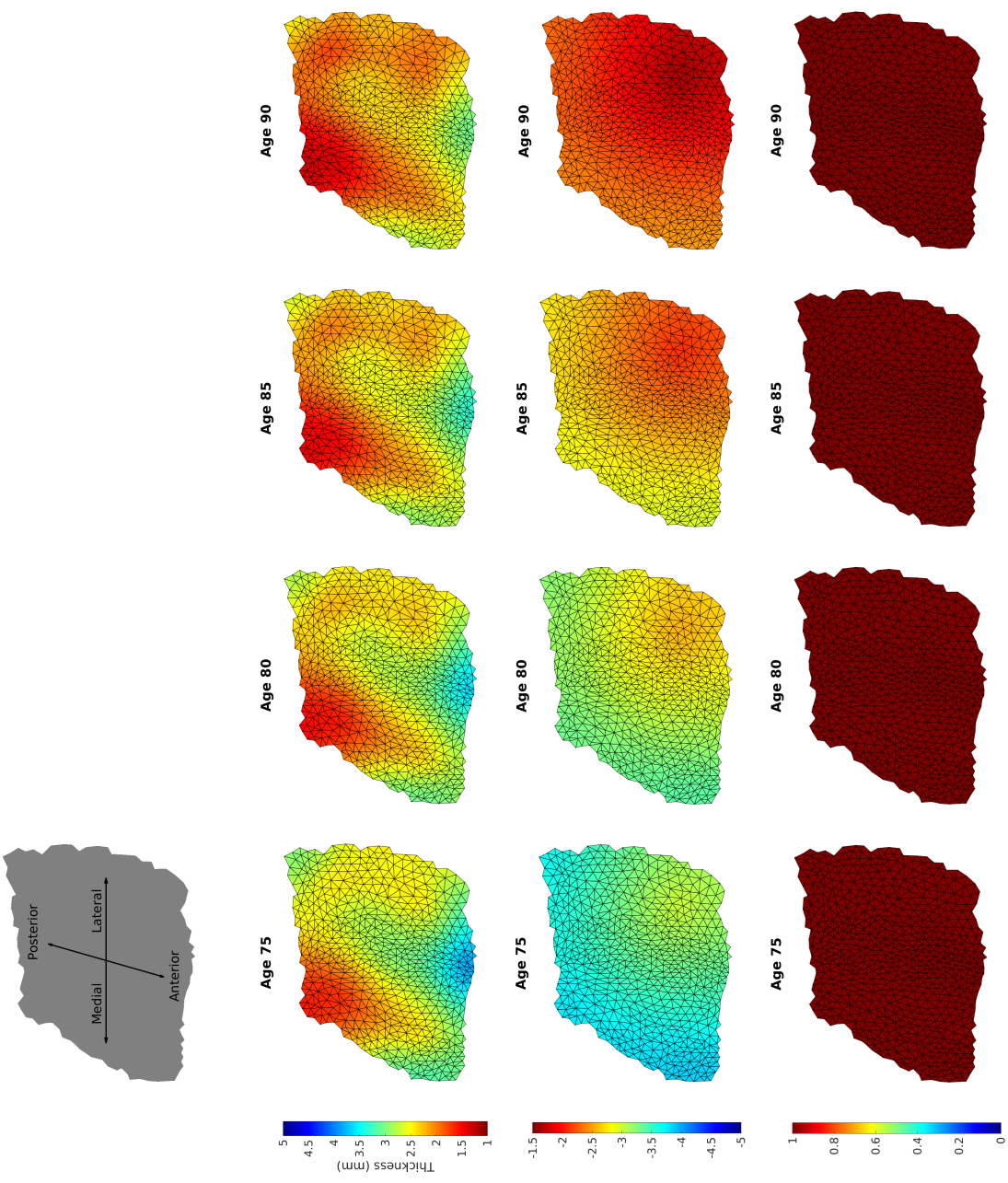

Figure 4.5: Simulation of AD using the model of atrophy spread. Cortical thickness (top), disease stage (middle), and local activity rate (bottom) over the rhinal cortex from age 75 to 90 in 5 year intervals. The surfaces are oriented such that left is medial, right is lateral, top is posterior, and bottom is anterior. Figure is reproduced with permission.[77]

observed cortical thickness:

$$f_n(x^n, \theta) = \begin{bmatrix} (M + \Delta t DS)^{-1}(Ma^n + \Delta t \kappa F(a^n)) \\ b^n + \lambda_1 \Delta t a^n \end{bmatrix} - x^{n+1},$$

$$f(x, \theta) = \begin{bmatrix} f_n(x^0, \theta) \\ \vdots \\ f_n(x^{N-1}, \theta) \end{bmatrix} = \mathbf{0}_{2MN \times 1}. \tag{4.21}$$

$$g(x, \theta) = \sum_{n=1}^{N} I_n ||\hat{\rho}^n - \rho^n||^2 \tag{4.22}$$

with indicator function:

$$I_n = \begin{cases} 1 & \text{if } \rho^n \text{ was measured} \\ 0 & \text{otherwise.} \end{cases}$$

The following excerpt is reproduced from the methods section in the publication of this model:[77]

> "We reformulate and numerically solve the optimization problem in its dual form, using the adjoint state method. To derive the differential change δx, we use $f(x, \theta) = 0$, implying that $\partial_\theta f(x, \theta)\delta\theta + \partial_x f(x, \theta)\delta x = 0$. The result takes the form:
>
> $$\delta x = -(\partial_x f(x, \theta))^{-1} \partial_\theta f(x, \theta)\delta\theta. \tag{4.23}$$
>
> Next, we define our energy function $J(\theta) = g(x, \theta)$. Recall that x is a column vector of x^n at time n, and that it is a function of θ. J is a function explicitly in terms of θ. To derive the gradient of the energy function, $\nabla J(\theta)$, we take the total derivative of $g(x, \theta)$:
>
> $$\partial_\theta J(\theta)\delta\theta = \partial_\theta g(x, \theta)\delta\theta + \partial_x g(x, \theta)\delta x.$$

Next, we substitute δx with [Eqn (4.23)]:

$$\partial_\theta J(\theta)\delta\theta \;=\; \partial_\theta g(x,\theta)\delta\theta \;+\; \partial_x g(x,\theta)(-(\partial_x f(x,\theta))^{-1}\partial_\theta f(x,\theta)\delta\theta).$$

Finally, divide both sides by $\delta\theta$ and take the transpose to see the result, shown in [Eqn (4.24)]:

$$\nabla J(\theta) \;=\; [\partial_\theta g(x,\theta) \;+\; \partial_x g(x,\theta)(-(\partial_x f(x,\theta))^{-1}\partial_\theta f(x,\theta)]^\intercal. \tag{4.24}$$

Based on this result, we introduce the adjoint state vector, p, shown below in [Eqn 4.25]:

$$p = -\partial_x g(x,\theta)(\partial_x f(x,\theta))^{-1}. \tag{4.25}$$

The explicit notation for this column vector p is the following:

$$p = \begin{bmatrix} p^1 \\ \vdots \\ p^N \end{bmatrix}, \quad p^n = \begin{bmatrix} p_1^n \\ \vdots \\ p_K^n \end{bmatrix}, \quad p_k^n = \begin{bmatrix} p_{a,k}^n \\ p_{b,k}^n \end{bmatrix}.$$

We are now ready to perform gradient descent. Given an initial guess for θ, calculate x iteratively from the initial time to the last observation time using the relationship $f(x,\theta) = 0$. Next, calculate the adjoint state vector p recursively starting from the last observation time back to the initial time, using the relationship below:

$$\begin{aligned} p^N &= [\partial_{x^N} g(x,\theta)]^\intercal, \\ p^n &= [\partial_{x^n} g(x,\theta) \;+\; (p^{n+1})^\intercal \;\partial_{x^n} f_n(x^n,\theta)]^\intercal. \end{aligned} \tag{4.26}$$

Finally, calculate the gradient $\nabla J(\theta)$ and update θ iteratively via gradient descent:

$$\nabla J(\theta) \;=\; [\partial_\theta g(x,\theta) \;+\; p^\intercal \;\partial_\theta f(x,\theta)]^\intercal. \tag{4.27}$$

The solution for ∇J in terms of variables a, b, p, θ; matrices M, S, F, dF; and constants λ_0, Δt, h is shown in [Equation 4.28]. As a reminder, mass matrix M of size $K \times K$, stiffness matrix S of size $K \times K$, and nonlinear reaction term F of size $K \times 1$ for K number of vertices have been explicitly defined in [Eqn 4.11], [Eqn 4.12], and [Eqn 4.13], respectively:

$$\nabla J = \begin{bmatrix} \partial_\kappa J & \partial_D J & \partial_{\lambda_1} J & \partial_{\bar{\rho}_{\max}} J & \partial_{c^0} J & \partial_{\bar{b}^0} J \end{bmatrix}^\intercal.$$

This gives us the system of equations for each discrete partial derivative:

$$
\begin{aligned}
\partial_\kappa J &= \sum_{n=0}^{N-1} (pa^{n+1})^\intercal (M + \Delta t D S)^{-1} (\Delta t F(a^n)), \\
\partial_D J &= \sum_{n=1}^{N-1} (pa^{n+1})^\intercal (M + \Delta t D S)^{-1} (\Delta t S)(M + \Delta t D S)^{-1} (Ma^n + \Delta t \kappa F(a^n)), \\
\partial_{\lambda_1} J &= \sum_{n=0}^{N-1} (pb^{n+1})^\intercal (\Delta t a^n), \\
\partial_{\bar{\rho}_{\max}} J &= \partial_{\bar{\rho}_{\max}} g \\
&= \sum_{n=0}^{N-1} 2 I_n (\bar{\rho}_{\max} h \circ \frac{e^{-\lambda_0 \Delta t n}}{1 + e^{b^n}} - \rho^n)(h \circ \frac{e^{-\lambda_0 \Delta t n}}{1 + e^{b^n}}), \\
\partial_{c^0} J &= \partial_{a^0} J \; \partial_{c^0} a^0 \\
&= \left((pa^1)^\intercal (M + \Delta t D S)^{-1} (M + \Delta t \kappa dF(a^0)) + (pb^1)^\intercal (\lambda_1 \Delta t) \right) \frac{r_k - c^0}{\sigma^2} a_k^0, \\
\partial_{\bar{b}^0} &= \sum_{k=1}^{K} p b_k^1.
\end{aligned}
\tag{4.28}
$$

where $r_k = \begin{bmatrix} r_{k,x} & r_{k,y} \end{bmatrix}$ for the location of a vertex k, and a_k^0 is a Gaussian distribution about center c^0 and fixed variance $\sigma^2 = 1$ evaluated at vertex k. The model implementation is available for download from `https://www.github.com/sue-kulason/FKPP`."

This concludes the derivation of the numerical optimization method that uses measures of cortical thickness over time to estimate the following parameters: reaction rate κ, diffusion rate D, disease intensity λ_1, average cortical thickness $\bar{\rho}_{\max}$, initial center of local activity c^0, and initial disease stage $\bar{b}^0$. Gradient descent is performed using MATLAB's fmincon function, supplied with the gradient calculated using the adjoint state method.

4.7 Parameter estimation: simulation analysis

The goal of this section is to determine how accurately parameters can be estimated on a simulation of AD generated from our atrophy spread model. The simulation from Section 4.5 generates cortical thickness measures from age 50 to 90. However, observing cortical thickness annually over 40 years is an unrealistic expectation for real data sets. Instead, we investigate how accurately parameters can be estimated under small windows of observation, and at different stages of the disease. First, we examine what fraction of randomly initialized runs accurately estimate all parameters. Then, we estimate a confidence interval of each parameter for a few specific cases.

We calculate the fraction of 100 randomly initialized runs that correctly estimate all parameters (up to two decimal places) when supplied with annual observations from a sliding window of 2, 5, and 10 years. We start each run from a randomly

selected set of parameters from the following ranges:

$$\kappa \in [0.01, 10],$$

$$D \in [0.01, 10],$$

$$\lambda_1 \in [0.1, 1],$$

$$b^0 \in [-10, -1],$$

$$\bar{\rho}_{\max} \in [2.64, 4.13].$$

For c^0, we selected points such that 95% of the volume under Gaussian a_0 overlapped with the rhinal cortex surface. This is a non-linear function that excludes points close to the surface boundary. Note that these are the same boundary constraints used in the numerical optimization problem.

Figure 4.6 shows the fraction of runs that correctly estimated all parameters under each condition. Early in the disease, prior to age 60, there is very little disease-related atrophy. The parameter estimation approach fails to accurately estimate parameters for short windows of observation in this early stage. As the window of observation slides toward the middle of the disease, we achieve a maximum accuracy of 91%, which is seen at age 70. In the late stage of the disease, this accuracy drops as it becomes more difficult to estimate initial cortical thickness, $\bar{\rho}_{\max}$, since observations begin after a substantial amount of atrophy has already occurred.

Next, we performed an analysis on the effect of disease stage on the confidence

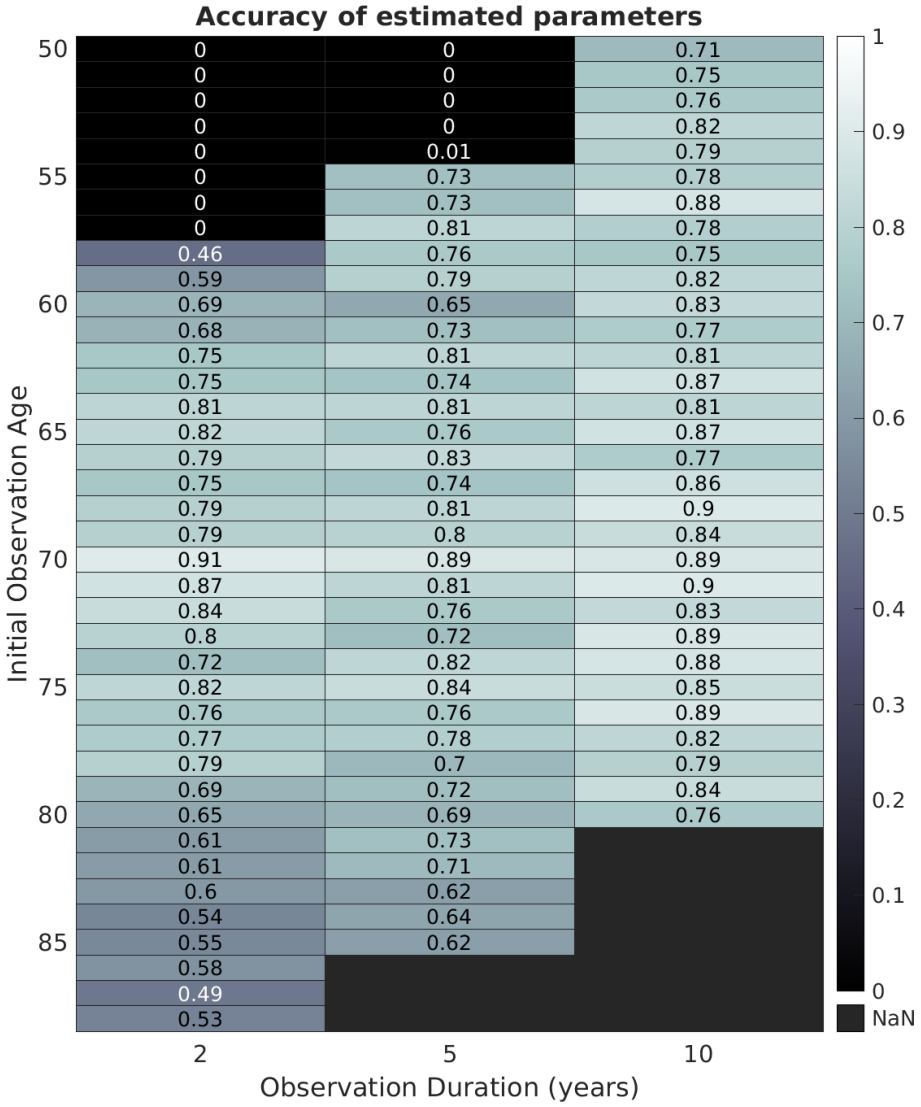

Figure 4.6: Fraction of 100 runs that succeeded in estimating the correct parameters over varying duration and observation start times. This figure has been reproduced with permission.[77]

intervals of parameters. We examine three cases: early stage, mid stage, and late stage. The early stage has a window of observation from age 55 to 60; the middle stage has a window of observation from age 70 to 75; and the late stage has a window of observation from age 85 to 90. The 90% confidence intervals of parameters and the radius that circumscribes 90% of c^0 can be calculated by first estimating the posterior distribution of the parameters. However, it is computationally intensive to sample directly from this distribution in this high-dimensional parameter space. Instead, we employ a Metropolis-Hastings algorithm to approximate the posterior distribution, $p(\theta \mid \rho_{\text{observed}})$, when given a set of observed cortical thicknesses, ρ_{observed}.

The following excerpt derives the method for calculating confidence intervals:[77]

> "We begin with the probability of observing ρ_{observed} given a set of parameters, as shown in [Eqn 4.29]. Note that $\rho(\theta)$ is shorthand for the model of atrophy spread with input parameters θ and output cortical thickness ρ:
>
> $$p(\rho_{\text{observed}} \mid \theta, \eta^2) = \frac{1}{(2\pi\eta^2)^{K/2}} \exp\left(-\frac{|\rho(\theta) - \rho_{\text{observed}}|^2}{2\eta^2}\right). \tag{4.29}$$
>
> We have introduced a nuisance parameter, η^2, which represents the noise associated with observations. We can approximate the distribution of η^2 as an inverse Wishart distribution with mean and variance 1, as shown in [Eqn 4.30]:
>
> $$p(\eta^2 \mid \alpha = 3,\ \beta = 2) = \frac{\beta^\alpha}{\Gamma(\alpha)} (\eta^2)^{-\alpha-1} \exp(-\frac{\beta}{\eta^2}). \tag{4.30}$$
>
> The values for β and α associated with an inverse Wishart distribution with mean and variance equal to 1 were derived by in the following way:

$$\begin{aligned}
\int p(\eta^2)d\eta^2 &= \int \frac{1}{\beta\Gamma(\alpha)}\left(\frac{\beta}{\eta^2}\right)^{\alpha+1}\exp(-\frac{\beta}{\eta^2})d\eta^2 = 1, \\
E[\eta^2] &= \int \eta^2 p(\eta^2)d\eta^2 = \int \frac{1}{\Gamma(\alpha)}\left(\frac{\beta}{\eta^2}\right)^{\alpha}\exp(-\frac{\beta}{\eta^2})d\eta^2 \\
&= \frac{\beta\Gamma(\alpha-1)}{\Gamma(\alpha)} = \frac{\beta}{\alpha-1}, \\
E[(\eta^2)^2] &= \int \left(\eta^2\right)^2 p(\eta^2)d\eta^2 = \int \frac{\beta}{\Gamma(\alpha)}\left(\frac{\beta}{\eta^2}\right)^{\alpha-1}\exp(-\frac{\beta}{\eta^2})d\eta^2 \\
&= \frac{\beta^2\Gamma(\alpha-2)}{\Gamma(\alpha)} = \frac{\beta^2}{(\alpha-1)(\alpha-2)}.
\end{aligned}$$

Setting the mean $E[\eta^2]\frac{\beta}{\alpha-1}$ equal to 1, we see that $\beta = \alpha - 1$. The variance $\text{var}(\eta^2) = E[(\eta^2)^2] - (E[\eta^2])^2$ is equal to $\frac{\beta^2}{(\alpha-1)(\alpha-2)} - \frac{\beta^2}{(\alpha-1)^2}$. Setting the variance to 1 and substituting $\beta = \alpha - 1$, we see that the variance is equal to $\frac{\beta^2}{(\alpha-1)^2(\alpha-2)} = \frac{1}{\alpha-2} = 1$, resulting in $\alpha = 3$, $\beta = 2$.

This approximation allows us to integrate for an explicit expression of a value proportional to the prior distribution $p(\theta \mid \rho_{\text{observed}})$ over K vertices, as derived below. We start by defining the joint probability $p(\rho_{\text{observed}}, \theta)$. Here, $p(\rho_{\text{observed}} \mid \theta, \eta^2)$ follows a Gaussian distribution, $p(\theta)$ is uniform across the parameter space, and $p(\eta^2)$ is approximated to be an inverse Wishart distribution with $\alpha = 3$, $\beta = 2$. Next, we see that the posterior distribution $p(\theta \mid \rho_{\text{observed}})$ is proportional to $p(\rho_{\text{observed}}, \theta)$:

$$\begin{aligned}
p(\rho_{\text{observed}}, \theta, \eta^2) &= p(\rho_{\text{observed}} \mid \theta, \eta^2)p(\theta)p(\eta^2), \\
p(\rho_{\text{observed}}, \theta) &= \int p(\rho_{\text{observed}} \mid \theta, \eta^2)p(\theta)p(\eta^2)d\eta^2, \\
p(\theta \mid \rho_{\text{observed}}) &= \frac{p(\rho_{\text{observed}}, \theta)}{\int p(\rho_{\text{observed}}, \theta')d\theta'} \propto p(\rho_{\text{observed}}, \theta).
\end{aligned}$$

By substituting the expressions for $p(\theta \mid \rho_{\text{observed}}, \eta^2)$, $p(\theta)$, and $p(\eta^2)$, we can express the posterior distribution of θ in terms of α, β, K, and ρ_{observed}, as shown in [Eqn 4.31]:

$$p(\theta \mid \rho_{\text{observed}}) \propto \int \frac{\beta^{\alpha}}{\Gamma(\alpha)}(\eta^2)^{-\alpha-1}\exp(-\frac{\beta}{\eta^2})\frac{1}{(2\pi\eta^2)^{K/2}} \exp\left(-\frac{|\rho(\theta)-\rho_{\text{observed}}|^2}{2\eta^2}\right)p(\theta)d\eta^2,$$

$$p(\theta \mid \rho_{\text{observed}}) \propto \int \frac{\beta^{\alpha}}{(2\pi)^{K/2}\Gamma(\alpha)}(\eta^2)^{-(\alpha+K/2+1)} \exp\left(-\frac{\beta+|\rho(\theta)-\rho_{\text{observed}}|/2}{\eta^2}\right)p(\theta)d\eta^2,$$

$$p(\theta \mid \rho_{\text{observed}}) \propto \frac{1}{(2\pi)^{K/2}}\frac{\beta^{\alpha}}{\Gamma(\alpha)}\frac{\Gamma(\alpha+K/2)}{(\beta+|\rho(\theta)-\rho_{\text{observed}}|/2)^{(\alpha+K/2)}},$$

$$p(\theta \mid \rho_{\text{observed}}) \propto \frac{1}{(\beta+|\rho(\theta)-\rho_{\text{observed}}|/2)^{(\alpha+K/2)}},$$

$$\hat{p}(\theta \mid \rho_{\text{observed}}) \propto \frac{1}{(\beta+|\rho(\theta)-\rho_{\text{observed}}|/2)^{(\alpha+K/2)}}. \tag{4.31}$$

We start from a random initial guess θ_0 in the parameter space. For each of $10,000$ iterations, we select a candidate $\hat{\theta}$ by updating the current θ with Gaussian noise of fixed variance. The variances were selected empirically to be: 0.01 for κ, 0.01 for D, 0.001 for λ_1, 0.01 for c^0 in the x and y direction, .05 for $\bar{b}_0$, and .005 for $\bar{\rho}_{\max}$. As shown in [Eqn 4.32], we update θ to $\hat{\theta}$ with a probability that is the ratio of the prior distribution at θ and $\hat{\theta}$, given $\alpha = 3$, $\beta = 2$, and observations ρ_{observed} for K vertices:

$$p_{\text{transition}}(\theta, \hat{\theta}, \rho_{\text{observed}}) = \min\left(\left(\frac{\beta+|\rho_{\text{observed}}-\rho(\theta)|^2/2}{\beta+|\rho_{\text{observed}}-\rho(\hat{\theta})|^2/2}\right)^{(\alpha+K/2)}, 1\right). \tag{4.32}$$

The 20,000 samples of θ are then used to calculate the 90% confidence intervals, and the radius of a circle that circumscribes 90% of c^0 values. ”

The radius that circumscribed 90% of c^0, as calculated from the posterior distribution of c^0, was 0.48 mm for early stage, 0.58 mm for middle stage, and 0.36 mm for late stage. These radii are relatively precise, small regions localized to the anterior lateral region of the rhinal cortex. For context, the rhinal cortex size is approximately

Parameter	Early Stage	Middle Stage	Late Stage
speed (mm/year)	(0.70, 1.38)	(0.77, 1.17)	(0.92, 1.05)
slope (1/mm)	(0.86, 1.78)	(0.88, 1.67)	(0.79, 1.12)
disease intensity	(0.06, 0.13)	(0.08, 0.11)	(0.07, 0.09)
disease stage	(-4.91, -5.41)	(-4.98, -5.66)	(-4.27, -4.95)
thickness (mm)	(3.37, 3.38)	(3.36, 3.38)	(3.37, 3.46)

Table 4.2: 90% confidence interval for 5-year annual windows of observation in the early, middle and late stage of the disease. Table has been reproduced with permission.[77]

20 mm wide (medial to lateral) and 25 mm long (anterior to posterior).

The 90% confidence intervals for each parameter are shown in Table 4.2. Speed, $\sqrt{\kappa D}$, had the widest confidence interval in the early stage before a substantial spread of atrophy could be observed, and the narrowest confidence interval in the late stage. Slope, $\sqrt{\frac{\kappa}{D}}$, also had the widest confidence interval in the early stage and narrowest confidence interval in the late stage. In addition, the confidence interval for speed was consistently narrower than for slope, suggesting that slope is a more difficult parameter to estimate accurately, regardless of the disease stage.

Similarly, the disease intensity, λ_1, had the widest confidence interval in the early stage and narrowest interval in the late stage. This makes intuitive sense because the confidence interval is the narrowest when the peak atrophy rate, and therefore disease intensity, is captured during the observation window. The confidence intervals are relatively narrow compared to speed and slope, as small changes in the disease intensity have a large effect on the outcome measure, cortical thickness.

Initial disease stage, $\bar{b}_0$, had the narrowest confidence interval in the early stage

and widest confidence interval in the late stage. The initial disease stage is more accurately estimated when the window of observation is closer to initialization age. Similarly, average cortical thickness prior to disease-related atrophy, $\bar{\rho}_{\max}$, had the smallest confidence interval in the early stage and the largest confidence interval in late stage. For both these parameters, the confidence interval is wider the further the observation window is from model initialization.

These results suggest that there is a trade-off between the accuracy of speed, slope, disease intensity (late stage is most accurate) versus disease stage and average cortical thickness prior to atrophy (early stage is most accurate). More generally, the parameters can be estimated accurately from the majority of random initial guesses when supplied with five or more years of annual observations. The wider confidence intervals for slope and disease stage suggest that these parameters are harder to estimate accurately.

4.8 Experimental results

We now apply parameter estimation and build confidence intervals of the parameters for three subjects. These three subjects were screened from the ADNI database to meet the following criteria:

- labeled a control at baseline
- remained a control for at least 8 years

- were scanned on 3T MRI for at least 5 years
- showed evidence of risk for MCI conversion
  - converted to MCI after 8 or more years
  - subjective memory complaint and amyloid positive
  - subjective memory complaint and impaired delayed recall when no amyloid data available

In addition, the MRIs included were required to have a consistent scan protocol across scans. This is to reduce concerns about difference in cortical thickness introduced by scan protocol changes. Table 4.3 shows the age, sex, and scan information of the subjects. Subject 1 was followed for 12 years and converted to MCI at year 9 or 10 (note that no diagnostic evaluation was performed at year 9). Subject 2 was followed for 9 years and did not convert to MCI during this period of observation, but show some evidence of AD. The subject was amyloid positive at baseline (as established by the ADNI Biospecimen Core) with an increasing subjective memory complaint (as measured by the Everyday Cognition Questionnaire). Subject 3 was followed for 11 years and did not convert to MCI during this period of observation, but also shows some evidence of AD. The subject had no CSF sample analyzed, so amyloid data was not be obtained. The subject had an increasing subjective memory complaint (as measured by the Everyday Cognition Questionnaire) and a delayed recall score significantly below the normal range on both the Logical Memory Subtest of

	Subject 1*	Subject 2	Subject 3
Age (years)	71.3	72.4	70.1
Number of Scans	10	8	9
Scan Period (years)	8.3	8.9	9.1
Follow-up Period (years)	12.1	8.9	10.6
Sex	F	F	M

Table 4.3: Demographic data (mean ± standard). *converted to MCI 9 or 10 years after the first scan. Note that the scan period is shorter than the follow-up period because accelerated 3T scans introduced in ADNI3 were excluded from analysis. Table has been reproduced with permission.[77]

the Wechsler Memory Scale (with a score as low as 7), and the Rey Auditory Verbal Learning Test (with a score as low as 2).

Figure 4.7, 4.8, and 4.9 show the cortical thickness measures over time calculated using the rhinal cortex pipeline described in Chapter 2. The bottom row of these figures show the change in cortical thickness over time for each subject. Subject 1 had a generally thinner cortex, but still showed the characteristic pattern of a thinner posterior region typically seen in the entorhinal cortex.[68] There is noticeable thinning over time in the anterior region of the rhinal cortex. Subject 2 starts with a thickness profile similar to the average stable NC. There is noticeable thinning over time in the lateral anterior region of the rhinal cortex, with particularly severe atrophy at the last scan time. Similarly, Subject 3 shows progressive thinning in the anterior lateral region of the rhinal cortex. While there is variation in the thickness profile from subject to subject, qualitatively, a consistent pattern of atrophy can be seen among these three subjects.

Unlike the NC average variation in thickness that was used to generate the disease

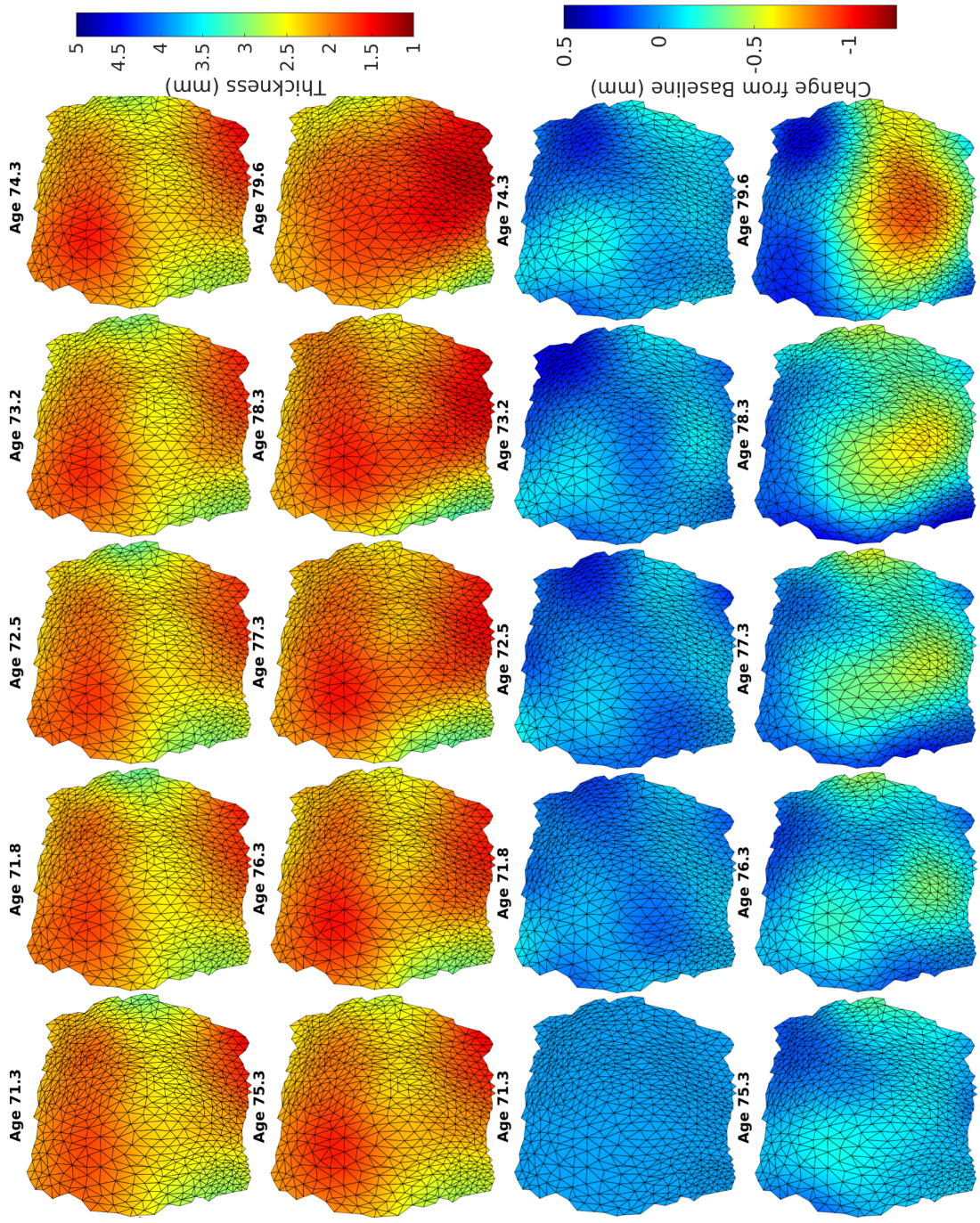

Figure 4.7: Measures of cortical thickness over time (top) and change in cortical thickness from the first scan (bottom) for Subject 1. The surfaces are oriented such that left is medial, right is lateral, top is posterior, and bottom is anterior. This figure has been modified and reproduced with permission.[77]

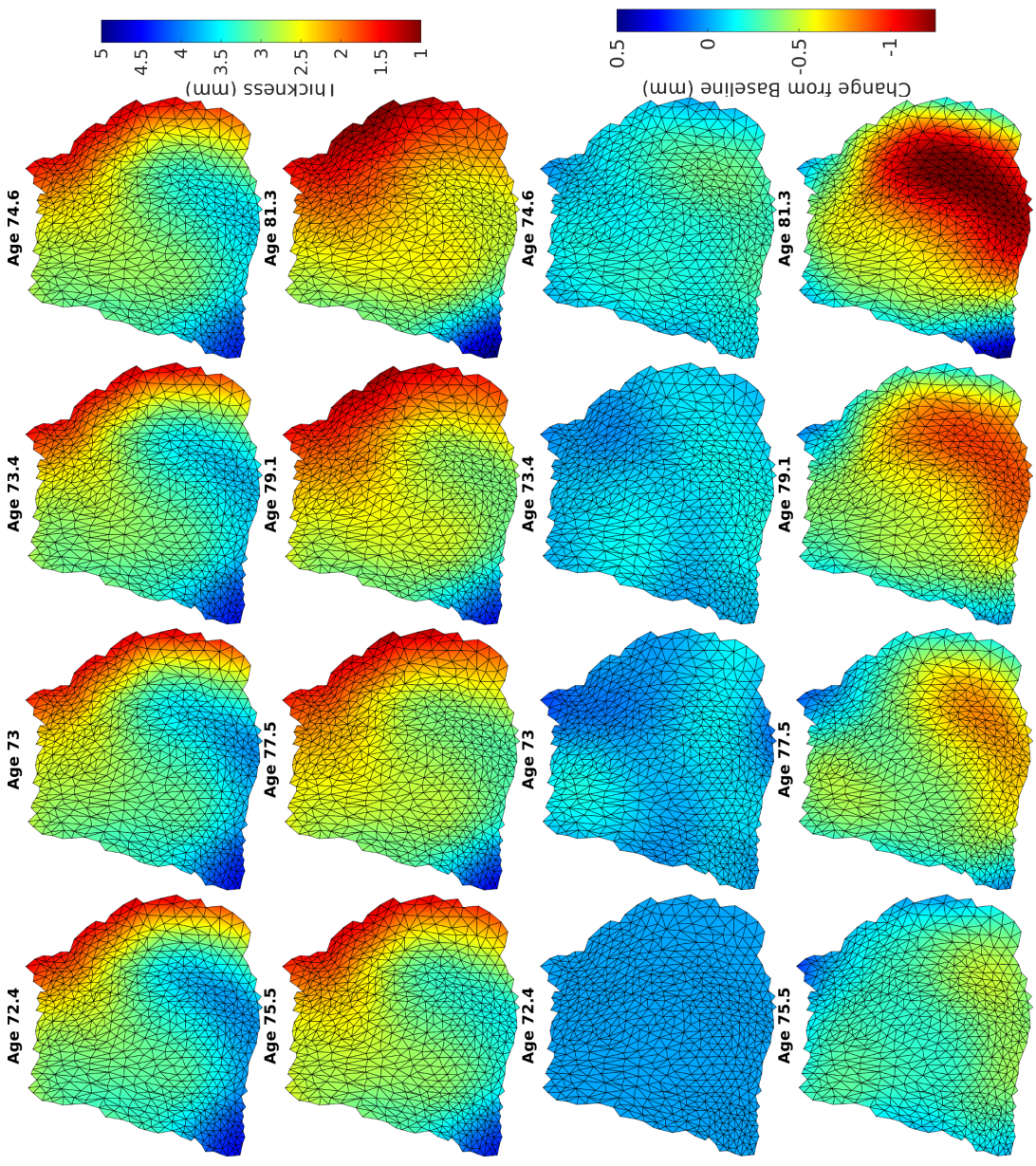

Figure 4.8: Measures of cortical thickness over time (top) and change in cortical thickness from the first scan (bottom) for Subject 2. The surfaces are oriented such that left is medial, right is lateral, top is posterior, and bottom is anterior. This figure has been modified and reproduced with permission.[77]

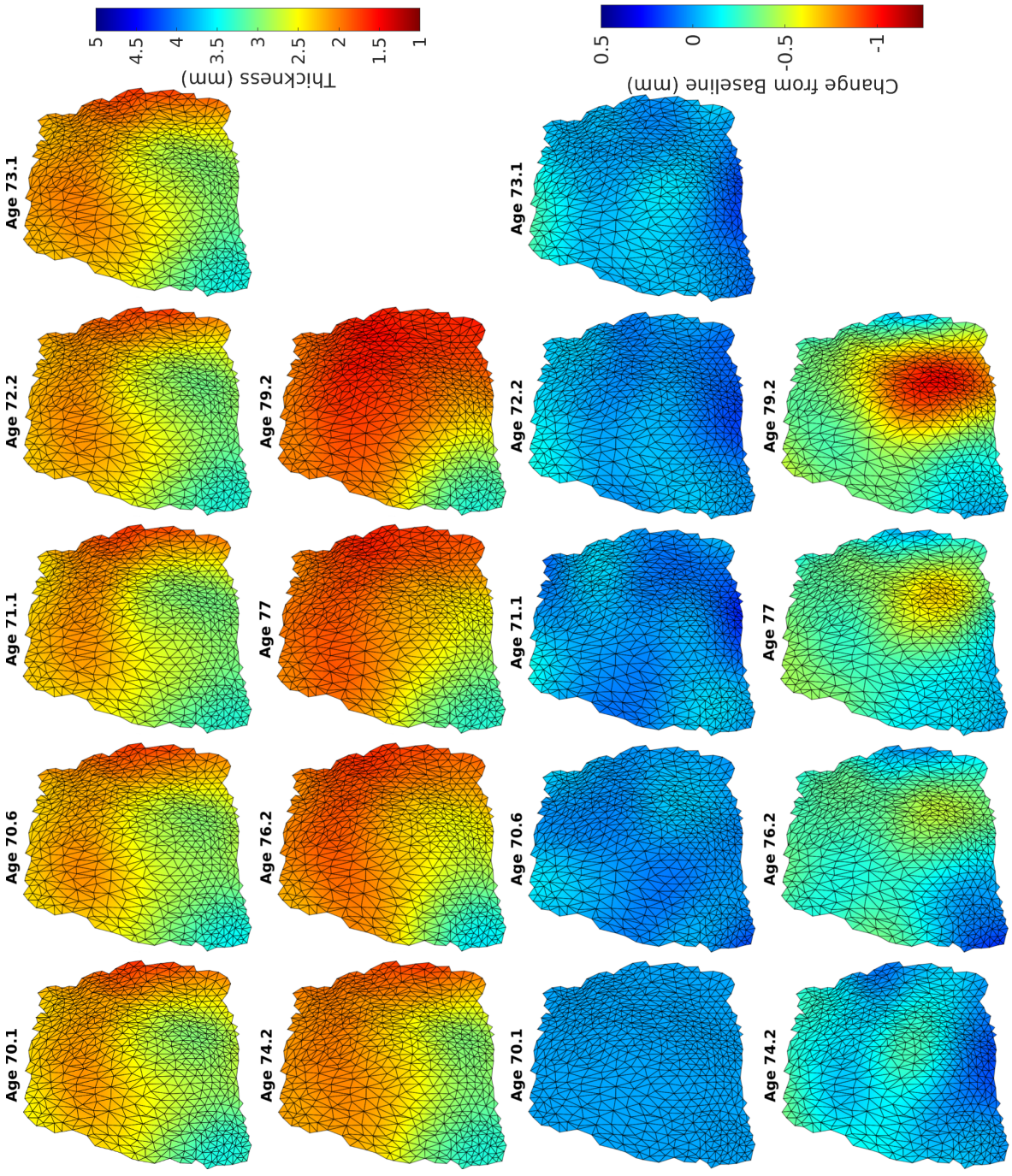

Figure 4.9: Measures of cortical thickness over time (top) and change in cortical thickness from the first scan (bottom) for Subject 3. The surfaces are oriented such that left is medial, right is lateral, top is posterior, and bottom is anterior. This figure has been modified and reproduced with permission.[77]

Parameter	Subject 1	Subject 2	Subject 3
speed (mm/year)	0.41	0.81	0.77
slope (1/mm)	0.56	2.06	5.36
disease intensity	0.38	0.26	0.32
atrophy origin	[-1.35, -2.29]	[-6.11, -1.58]	[-3.17, -0.49]
disease stage	-5.66	-8.23	-9.96
thickness (mm)	2.72	3.66	3.01

Table 4.4: MAP estimate of parameters for Subjects 1, 2, and 3. This figure has been reproduced with permission.[77]

simulation, we estimated variation in cortical thickness for the subjects based on the cortical thickness profile of their first scan. The 3 subjects were individuals who did not convert to MCI within 8 years of the first scan. Since disease-related atrophy is thought to begin 8 to 10 years prior to symptom onset, the shape of the cortex at the first scan is a reasonable approximation of the cortical thickness prior to disease-related atrophy.[70,88]

The best (maximum a priori) estimator of parameters from 100 randomly initialized runs are shown in Table 4.4. All three subjects had an atrophy origin, c^0, in the anterior lateral quadrant of the rhinal cortex. The speed of spread was somewhat consistent between subjects, varying from 0.41 mm/year and 0.81 mm/year. The disease intensity also seemed to be relatively consistent between subjects, varying from 0.26 to 0.38. The slope and disease stage varied more widely, as did the initial average cortical thickness, $\bar{\rho}_{\max}$. This variation in cortical thickness and disease stage is expected based on the results from analyzing the simulation. The window of observation begins around age 70 for these subjects.

Parameter	Subject 1	Subject 2	Subject 3
speed (mm/year)	(0.38, 0.47)	(0.78, 0.95)	(0.67, 0.97)
slope (1/mm)	(0.47, 0.65)	(1.56, 2.76)	(4.09, 6.34)
disease intensity	(0.30, 0.43)	(0.25, 0.27)	(0.31, 0.32)
disease stage	(-5.36, -5.88)	(-7.82, -8.62)	(-9.52, -9.99)
thickness (mm)	(2.70, 2.75)	(3.64, 3.69)	(2.99, 3.03)

Table 4.5: 90% confidence interval for Subjects 1, 2, and 3. This figure has been reproduced with permission.[77]

90% confidence intervals and radius circumscribing 90% of c^0 were calculated using the Metropolis-Hastings algorithm that was described in detail in Section 4.7. The radius that circumscribed 90% of the atrophy origin, c^0, was 0.61 mm for Subject 1, 0.59 mm for Subject 2, and 0.61 mm for Subject 3.

Table 4.5 shows the 90% confidence intervals. The radius for atrophy origin and the confidence interval for speed, disease intensity, and average cortical thickness were relatively narrow in all three subjects. Slope and initial disease stage had somewhat larger confidence intervals. In particular, the estimates for slope varied quite a lot between the subjects.

The initial disease stage is largest in Subject 1 and smallest for Subject 3. While the value of $\bar{b}_0$ has a wider confidence interval, the ordering of disease stage among the three subjects corresponds to the available diagnostic data. These subjects are separated only by a year in age, and Subject 1 converted to MCI 9 or 10 years after the baseline scan. Subject 3 has yet to convert after 11 years.

These findings suggest that the model may have some utility estimating parameters such as the origin of atrophy, speed, and the disease stage. While three subjects

is too small a set to draw rigorous conclusions, the evidence suggests that the initial site of atrophy is consistently in the anterior lateral region of the rhinal cortex, and spreads at a speed less than 1 mm per year. The disease stage may be particularly useful for identifying a subject's current stage in the disease, and rectify the variability seen in staging based on histopathological evidence versus staging based on clinical evidence.

4.9 Summary

In this chapter we have introduced a new, biologically-inspired model of atrophy spread for individual subjects. We used the model to generate a simulation of AD-related atrophy across the rhinal cortex. We then introduced a technique to estimate model parameters and their confidence intervals based on observed cortical thicknesses over a period of time. Finally, we examined a few subjects that were followed for 8 or more years during the preclinical phase of AD.

Parameter estimation results on the disease simulation suggest that we can obtain accurate estimates of parameters when given a window of 5 or more years of annual observations. The accuracy falls when supplied 2 years of annual observations, but only in the very early and very late stages of the disease.

In the three case studies of subject data, the origin of atrophy was detected in the anterior lateral region of the rhinal cortex. This finding is consistent with our

previous population analyses of preclinical AD, discussed in Chapter 3.

This is the first model, to our knowledge, that examines the speed of atrophy over the progression of a neurodegenerative diseases. The speed of spread averaged 0.66 mm per year across the three subjects, and had a relatively narrow confidence interval that had an upper bound less than 1 mm per year.

There are a few other considerations for future work on this atrophy spread model. As currently written, the model assumes uniform spread of atrophy. However, it is not known whether atrophy spreads uniformly or whether there is some bias. For example, atrophy may spread faster medial to lateral than it does anterior to posterior. Adding this type of flexibility to the model may make parameter estimation a more difficult problem, but with the potential for more accurate results.

Another area of focus is the estimation of the cortical thickness profile prior to disease-related atrophy. In the subjects examined in Section 4.8, the cortical thickness was estimated based on the first scan. This is not a strategy that can be employed on subjects with a shorter duration of observation, since it will not be known whether disease-related atrophy has already occurred by the time of the first scan. Developing a subject-specific prior of cortical thickness is a topic of interest since collateral sulcus location and cortical thickness vary greatly, even among healthy subjects.

Chapter 5

General discussion

5.1 Contributions

In this thesis, we developed a set of methods to 1) examine where grey matter atrophy occurs, 2) when atrophy begins, and 3) how fast atrophy spreads, based on time-series MRI data. We used these methods to characterize Alzheimer's disease in the rhinal cortex during the preclinical stage, prior to onset of mild cognitive impairment.

Analyzing preclinical subjects, whose disease trajectories are unknown at the time of data acquisition, has been made possible through the collection of big data sets. By carefully selecting subjects based on a strict set of diagnostic inclusion criteria, accounting for anatomical variations in folding patterns, and leveraging longitudinal MRI data, we can characterize the pattern of atrophy in the earliest stages of

Alzheimer's disease.

This work builds on the foundations of computational anatomy, which allow us to localize and quantify shape changes across subjects. Our analyses of preclinical Alzheimer's disease subjects show evidence of atrophy that begins in the anterior transentorhinal cortex at least 9 years prior to diagnosis of mild cognitive impairment. Atrophy is then detected later in the entorhinal cortex. In addition, the rate of atrophy in subjects after diagnosis of mild cognitive impairment is significantly faster, which suggests that the speed of atrophy increases as the disease progresses. It is therefore important to identify patients in this period of slow atrophy prior to symptom onset, and prior to increased rate of atrophy. Finally, our subject-specific work suggests that the spread of atrophy spread may be less than 1 mm per year, beginning in the anterior transentorhinal cortex, during this preclinical stage. This type of personalized, patient-specific modeling is a budding field with potential for increased sensitivity to disease-related changes and individualized care.

Recently, there has also been a trend toward standardizing subregional boundaries of the brain. Extensive efforts have focused on the hippocampal formation, but have not yet addressed the rhinal cortex. Since researchers use many different boundary definitions for the rhinal cortex, we harmonized several atlases so that the results are accessible to several disciplines within the neuroscience community. Specifically, the pipeline in this work mapped results to atlases using macro-structural landmarks, functional connectivity landmarks, and histological landmarks. The goal was for the

results to be interpreted by a wider audience.

5.2 Limitations

The findings presented in this thesis are based on relatively small sample sizes. Creating accurate manual segmentations of the rhinal cortex is a time consuming process. As such, it is difficult to scale up this method to larger sample sizes. While automatic methods scale well, segmentation accuracy is often sacrificed. In particular, the entorhinal cortex is difficult to segment automatically due to its proximity to the meninges and oculomotor nerve, which are of a similar intensity to gray matter voxels in T1 scans. Furthermore, the transentorhinal cortex is a region with highly variant folding patterns that may not be captured in the atlas, leading to systematic bias in automatic segmentation. This may explain, in part, why many neuroimaging studies have focused on the hippocampus rather than the rhinal cortex. The hippocampus can more reliably be segmented using automated approaches, making large-scale studies easier to conduct.

Another limitation is introduced in the change-point analysis utilizing data from ADNI. In this database, the samples were collected to meet a fixed sample size for each diagnostic group, which biases the distribution of diagnostic grouping. In addition, the follow-up period varied from two years to thirteen years. This issue is mitigated by the use of distribution estimates calculated from the BIOCARD database, where

samples were not collected to meet fixed samples sizes based on diagnostic criteria.

Finally, there are very few subjects that are followed and imaged 8 or more years prior to a diagnosis of mild cognitive impairment. This limits the sample size available for subject-specific modeling, and may also bias toward subjects that show symptoms later in their disease course. As methods to develop a prior on subject-specific cortical thickness improve, it may be possible to examine subjects followed over a shorter duration.

5.3 Future directions

It is of interest to develop metrics of disease progression that are robust to natural variation in folding in the transentorhinal cortex. Therefore, one future direction will be to extend the analyses presented here to a set of subjects with shallow, discontinuous variants of the collateral sulcus. Autopsy studies have shown that subjects with a shallow, discontinuous CoS have a TEC that begins at the deepest extent of the CoS and extends out laterally, whereas deep, continuous CoS have a TEC that begins at the shoulder of the CoS and extends only to the deepest extent of the CoS,[67].[69] It may be possible to incorporate this type of information in a multi-atlas segmentation or classification approach with CoS variant-specific atlases to delineate for the rhinal cortex.

In addition, some recent work has been done to address the entorhinal proximity to

meninges using a multi-atlas approach, where atlases have T1 and T2 scans manually segmented.[108] It remains to be seen whether this type of automated approach affects entorhinal and transentorhinal metrics that were produced in this dissertation.

In the next 5 years, as more high-resolution T2 data becomes available, it will be possible to extend these analyses to the subregions of the hippocampal formation. Of particular interest is when atrophy can be detected in the CA1 subregion compared to the rhinal cortex, and whether this pattern of atrophy can be used to stage the progression of the disease.

Finally, the accuracy of subject-specific modeling stands to improve with an accurate prior of cortical thickness before age-related and disease-related atrophy. This type of prior would allow us to examine subjects that have disease-related atrophy at the time of scanning, greatly increasing the sample size. Separating natural variation in thickness from disease-related changes will be essential for monitoring disease progression accurately.

5.4 Conclusions

This thesis provides a framework for analyzing time-series MRI data in neurodegenerative diseases, with a focus on Alzheimer's disease. We show strong evidence that significant disease-related atrophy occurs in the anterior transentorhinal cortex and entorhinal cortex prior to a change in cognitive status. Disease-related atrophy

begins at least 9 years prior to a clinical diagnosis of mild cognitive impairment, and begins in the transentorhinal cortex before spreading to the entorhinal cortex. Subject-specific modeling work located the origin of atrophy and speed of atrophy consistently among subjects, which was demonstrated to be under 1 mm per year in the anterior transentorhinal cortex. Both the population-level analyses and subject-specific modeling may prove useful for staging early progression of Alzheimer's and characterizing disease spread.

Bibliography

[1] L. E. Hebert, J. Weuve, P. A. Scherr, and D. A. Evans, "Alzheimer disease in the United States (2010–2050) estimated using the 2010 census," *Neurology*, vol. 80, no. 19, pp. 1778–1783, 2013.

[2] G. M. McKhann, D. S. Knopman, H. Chertkow, B. T. Hyman, C. R. Jack Jr, C. H. Kawas, W. E. Klunk, W. J. Koroshetz, J. J. Manly, R. Mayeux *et al.*, "The diagnosis of dementia due to Alzheimer's disease: recommendations from the National Institute on Aging-Alzheimer's Association workgroups on diagnostic guidelines for Alzheimer's disease," *Alzheimer's & Dementia*, vol. 7, no. 3, pp. 263–269, 2011.

[3] B. D. James, R. S. Wilson, P. A. Boyle, J. Q. Trojanowski, D. A. Bennett, and J. A. Schneider, "TDP-43 stage, mixed pathologies, and clinical Alzheimers-type dementia," *Brain*, vol. 139, no. 11, pp. 2983–2993, 2016.

[4] A. Serrano-Pozo, J. Qian, S. E. Monsell, D. Blacker, T. Gómez-Isla, R. A. Betensky, J. H. Growdon, K. A. Johnson, M. P. Frosch, R. A. Sperling *et al.*, "Mild

to moderate Alzheimer dementia with insufficient neuropathological changes," *Annals of neurology*, vol. 75, no. 4, pp. 597–601, 2014.

[5] A. Kapasi, C. DeCarli, and J. A. Schneider, "Impact of multiple pathologies on the threshold for clinically overt dementia," *Acta Neuropathol*, vol. 134, no. 2, pp. 171–186, 2017.

[6] P. T. Nelson, E. Head, F. A. Schmitt, P. R. Davis, J. H. Neltner, G. A. Jicha, E. L. Abner, C. D. Smith, L. J. Van Eldik, R. J. Kryscio *et al.*, "Alzheimers disease is not "brain aging": neuropathological, genetic, and epidemiological human studies," *Acta Neuropathol*, vol. 121, no. 5, pp. 571–587, 2011.

[7] L. A. Klatka, R. B. Schiffer, J. M. Powers, and A. M. Kazee, "Incorrect diagnosis of Alzheimer's disease: a clinicopathologic study," *Archives of neurology*, vol. 53, no. 1, pp. 35–42, 1996.

[8] M. S. Albert, S. T. DeKosky, D. Dickson, B. Dubois, H. H. Feldman, N. C. Fox, A. Gamst, D. M. Holtzman, W. J. Jagust, R. C. Petersen *et al.*, "The diagnosis of mild cognitive impairment due to Alzheimer's disease: recommendations from the National Institute on Aging-Alzheimer's Association workgroups on diagnostic guidelines for Alzheimer's disease," *Alzheimer's & Dementia*, vol. 7, no. 3, pp. 270–279, 2011.

[9] J. A. Schneider, Z. Arvanitakis, S. E. Leurgans, and D. A. Bennett, "The

neuropathology of probable Alzheimer disease and mild cognitive impairment," *Annals of Neurology*, vol. 66, no. 2, pp. 200–208, 2009.

[10] E. L. Abner, R. J. Kryscio, F. A. Schmitt, D. W. Fardo, D. C. Moga, E. T. Ighodaro, G. A. Jicha, L. Yu, H. H. Dodge, C. Xiong *et al.*, "Outcomes after diagnosis of mild cognitive impairment in a large autopsy series," *Annals of neurology*, vol. 81, no. 4, pp. 549–559, 2017.

[11] R. A. Sperling, P. S. Aisen, L. A. Beckett, D. A. Bennett, S. Craft, A. M. Fagan, T. Iwatsubo, C. R. Jack Jr, J. Kaye, T. J. Montine *et al.*, "Toward defining the preclinical stages of Alzheimers disease: Recommendations from the National Institute on Aging-Alzheimer's Association workgroups on diagnostic guidelines for Alzheimer's disease," *Alzheimer's & Dementia*, vol. 7, no. 3, pp. 280–292, 2011.

[12] H. Braak and E. Braak, " Neuropathological stageing of Alzheimer-related changes," *Acta Neuropathol*, vol. 4, no. 82, pp. 239–259, 1991.

[13] P. V. Arriagada, J. H. Growdon, E. T. Hedley-Whyte, and B. T. Hyman, "Neurofibrillary tangles but not senile plaques parallel duration and severity of Alzheimer's disease," *Neurology*, vol. 42, no. 3, pp. 631–631, 1992.

[14] S. E. Arnold, B. T. Hyman, J. Flory, A. R. Damasio, and G. W. Van Hoesen, "The topographical and neuroanatomical distribution of neurofibrillary tangles

and neuritic plaques in the cerebral cortex of patients with alzheimer's disease," *Cerebral cortex*, vol. 1, no. 1, pp. 103–116, 1991.

[15] S. Kuzuhara, Y. Ihara, Y. Toyokura, and H. Shimada, "A semiquantitative study on Alzheimer neurofibrillary tangles demonstrated immunohistochemically with anti-tau antibodies, in the brains of non-demented and demented old people," *Brain and nerve*, vol. 41, no. 5, pp. 465–470, 1989.

[16] J. C. Morris and J. L. Price, "Pathologic correlates of nondemented aging, mild cognitive impairment, and early-stage Alzheimers disease," *Journal of Molecular Neuroscience*, vol. 17, no. 2, p. 101, 2001.

[17] J. F. Crary, J. Q. Trojanowski, J. A. Schneider, J. F. Abisambra, E. L. Abner, I. Alafuzoff, S. E. Arnold, J. Attems, T. G. Beach, E. H. Bigio *et al.*, "Primary age-related tauopathy (PART): a common pathology associated with human aging," *Acta Neuropathol*, vol. 128, no. 6, pp. 755–766, 2014.

[18] K. Tsuchiya and K. Kosaka, "Neuropathological study of the amygdala in presenile Alzheimer's disease," *Journal of the neurological sciences*, vol. 100, no. 1-2, pp. 165–173, 1990.

[19] L. M. Shaw, H. Vanderstichele, M. Knapik-Czajka, C. M. Clark, P. S. Aisen, R. C. Petersen, K. Blennow, H. Soares, A. Simon, P. Lewczuk *et al.*, "Cerebrospinal fluid biomarker signature in alzheimer's disease neuroimaging initiative subjects," *Annals of neurology*, vol. 65, no. 4, pp. 403–413, 2009.

[20] B. Olsson, R. Lautner, U. Andreasson, A. Öhrfelt, E. Portelius, M. Bjerke, M. Hölttä, C. Rosén, C. Olsson, G. Strobel *et al.*, "CSF and blood biomarkers for the diagnosis of Alzheimer's disease: a systematic review and meta-analysis," *The Lancet Neurology*, vol. 15, no. 7, pp. 673–684, 2016.

[21] W. Jagust, "Positron emission tomography and magnetic resonance imaging in the diagnosis and prediction of dementia," *Alzheimer's & Dementia*, vol. 2, no. 1, pp. 36–42, 2006.

[22] K. Kantarci and C. R. Jack, "Neuroimaging in Alzheimer disease: an evidence-based review," *Neuroimaging Clinics*, vol. 13, no. 2, pp. 197–209, 2003.

[23] T. Gómez-Isla, R. Hollister, H. West, S. Mui, J. H. Growdon, R. C. Petersen, J. E. Parisi, and B. T. Hyman, "Neuronal loss correlates with but exceeds neurofibrillary tangles in Alzheimer's disease," *Annals of Neurology: Official Journal of the American Neurological Association and the Child Neurology Society*, vol. 41, no. 1, pp. 17–24, 1997.

[24] T. Arendt, J. T. Stieler, and M. Holzer, "Tau and tauopathies," *Brain research bulletin*, vol. 126, pp. 238–292, 2016.

[25] M. Atiya, B. T. Hyman, M. S. Albert, and R. Killiany, "Structural magnetic resonance imaging in established and prodromal Alzheimer disease: a review," *Alzheimer Dis Assoc Disord*, vol. 17, no. 3, pp. 177–195, 2003.

[26] K. Kantarci and C. R. Jack, "Quantitative magnetic resonance techniques as surrogate markers of Alzheimer's disease," *NeuroRx*, vol. 1, no. 2, pp. 196–205, 2004.

[27] D. Devanand, G. Pradhaban, X. Liu, A. Khandji, S. De Santi, S. Segal, H. Rusinek, G. Pelton, L. Honig, R. Mayeux *et al.*, "Hippocampal and entorhinal atrophy in mild cognitive impairment: prediction of Alzheimer disease," *Neurology*, vol. 68, no. 11, pp. 828–836, 2007.

[28] Kerchner, G. A. and Deutsch, G. K. and Zeineh, M. and Doughterty, R. F. and Saranathan, M. and Rutt, B. K., "Hippocampal CA1 apical neuropil atrophy and memory performance in Alzheimer's disease," *Neuroimage*, vol. 63, no. 1, pp. 194–202, 2012.

[29] D. Devanand, R. Bansal, J. Liu, X. Hao, G. Pradhaban, and B. S. Peterson, "MRI hippocampal and entorhinal cortex mapping in prediction conversion to Alzheimer's disease," *Neuroimage*, vol. 60, no. 3, pp. 1622–1629, 2012.

[30] S. Durrleman, T. Fletcher, G. Gerig, and M. Niethammer, *Spatio-temporal Image Analysis for Longitudinal and Time-Series Image Data: Second International Workshop, STIA 2012, Held in Conjunction with MICCAI 2012, Nice, France, October 1, 2012, Proceedings*. Springer, 2012, vol. 7570.

[31] M. I. Miller, L. Younes, J. T. Ratnanather, T. Brown, H. Trinh, E. Postell, D. S. Lee, M.-C. Wang, S. Mori, R. O'Brien *et al.*, "The diffeomorphometry

of temporal lobe structures in preclinical Alzheimer's disease," *NeuroImage: Clinical*, vol. 3, pp. 352–360, 2013.

[32] B. Dickerson, T. Stoub, R. Shah, R. Sperling, R. Killiany, M. Albert, B. Hyman, D. Blacker, and L. Detoledo-Morrell, "Alzheimer-signature MRI biomarker predicts AD dementia in cognitively normal adults," *Neurology*, vol. 76, no. 16, pp. 1395–1402, 2011.

[33] C. Pettigrew, A. Soldan, Y. Zhu, M.-C. Wang, A. Moghekar, T. Brown, M. Miller, and M. Albert, "Cortical thickness in relation to clinical symptom onset in preclinical AD," *NeuroImage: Clinical*, vol. 12, pp. 116–122, 2016.

[34] L. G. Apostolova, L. Mosconi, P. M. Thompson, A. E. Green, K. S. Hwang, A. Ramirez, R. Mistur, W. H. Tsui, and M. J. de Leon, "Subregional hippocampal atrophy predicts Alzheimer's dementia in the cognitively normal," *Neurobiology of aging*, vol. 31, no. 7, pp. 1077–1088, 2010.

[35] T. den Heijer, M. I. Geerlings, F. E. Hoebeek, A. Hofman, P. J. Koudstaal, and M. M. Breteler, "Use of hippocampal and amygdalar volumes on magnetic resonance imaging to predict dementia in cognitively intact elderly people," *Archives of general psychiatry*, vol. 63, no. 1, pp. 57–62, 2006.

[36] C. R. Jack, M. M. Shiung, J. L. Gunter, P. C. Obrien, S. D. Weigand, D. S. Knopman, B. F. Boeve, R. J. Ivnik, G. E. Smith, R. H. Cha *et al.*, "Comparison

of different MRI brain atrophy rate measures with clinical disease progression in AD," *Neurology*, vol. 62, no. 4, pp. 591–600, 2004.

[37] A. Soldan, C. Pettigrew, Y. Lu, M.-C. Wang, O. Selnes, M. Albert, T. Brown, J. T. Ratnanather, L. Younes, M. I. Miller *et al.*, "Relationship of medial temporal lobe atrophy, APOE genotype, and cognitive reserve in preclinical A lzheimer's disease," *Human brain mapping*, vol. 36, no. 7, pp. 2826–2841, 2015.

[38] J. G. Csernansky, L. Wang, J. Swank, J. P. Miller, M. Gado, D. McKeel, M. Miller, and J. C. Morris, "Preclinical detection of Alzheimer's disease: hippocampal shape and volume predict dementia onset in the elderly," *Neuroimage*, vol. 25, no. 3, pp. 783–792, 2005.

[39] U. Grenander and M. I. Miller, "Computational anatomy: An emerging discipline," *Quarterly of applied mathematics*, vol. 56, no. 4, pp. 617–694, 1998.

[40] M. I. Miller, A. Trouvé, and L. Younes, "On the metrics and Euler-Lagrange equations of computational anatomy," *Annual review of biomedical engineering*, vol. 4, no. 1, pp. 375–405, 2002.

[41] M. F. Beg, M. I. Miller, A. Trouvé, and L. Younes, "Computing large deformation metric mappings via geodesic flows of diffeomorphisms," *Int J Comput Vis*, vol. 61, no. 2, pp. 139–157, 2005.

[42] M. Vaillant and J. Glaunès, "Surface matching via currents," in *Biennial International Conference on Information Processing in Medical Imaging*. Springer, 2005, pp. 381–392.

[43] N. Charon and A. Trouvé, "The varifold representation of nonoriented shapes for diffeomorphic registration," *SIAM Journal on Imaging Sciences*, vol. 6, no. 4, pp. 2547–2580, 2013.

[44] J. Glaunès, A. Qiu, M. I. Miller, and L. Younes, "Large deformation diffeomorphic metric curve mapping," *International journal of computer vision*, vol. 80, no. 3, p. 317, 2008.

[45] C. Ceritoglu, X. Tang, M. Chow, D. Hadjiabadi, D. Shah, T. Brown, M. H. Burhanullah, H. Trinh, J. Hsu, K. A. Ament *et al.*, "Computational analysis of LDDMM for brain mapping," *Frontiers in neuroscience*, vol. 7, p. 151, 2013.

[46] J. Zhang, Q. Peng, Q. Li, N. Jahanshad, Z. Hou, M. Jiang, N. Masuda, D. R. Langbehn, M. I. Miller, S. Mori *et al.*, "Longitudinal characterization of brain atrophy of a Huntington's disease mouse model by automated morphological analyses of magnetic resonance images," *Neuroimage*, vol. 49, no. 3, pp. 2340–2351, 2010.

[47] A. Qiu, J. Zhong, S. Graham, M. Y. Chia, and K. Sim, "Combined analyses of thalamic volume, shape and white matter integrity in first-episode schizophrenia," *Neuroimage*, vol. 47, no. 4, pp. 1163–1171, 2009.

[48] A. Qiu, C. Fennema-Notestine, A. M. Dale, M. I. Miller, and Alzheimer's Disease Neuroimaging Initiative, "Regional shape abnormalities in mild cognitive impairment and Alzheimer's disease," *Neuroimage*, vol. 45, no. 3, pp. 656–661, 2009.

[49] D. J. Tward, C. S. Sicat, T. Brown, A. Bakker, M. Gallagher, M. Albert, and M. I. Miller, "Entorhinal and transentorhinal atrophy in mild cognitive impairment using longitudinal diffeomorphometry," *Alzheimers Dement*, vol. 9, pp. 41–50, 2017.

[50] A. Du, N. Schuff, J. Kramer, S. Ganzer, X. Zhu, W. Jagust, B. Miller, B. R. Reed, D. Mungas, K. Yaffe *et al.*, "Higher atrophy rate of entorhinal cortex than hippocampus in AD," *Neurology*, vol. 62, no. 3, pp. 422–427, 2004.

[51] A. M. Winkler, P. Kochunov, J. Blangero, L. Almasy, K. Zilles, P. T. Fox, R. Duggirala, and D. C. Glahn, "Cortical thickness or grey matter volume? The importance of selecting the phenotype for imaging genetics studies," *Neuroimage*, vol. 53, no. 3, pp. 1135–1146, 2010.

[52] B. C. Dickerson and D. Wolk, "Biomarker-based prediction of progression in MCI: comparison of AD-signature and hippocampal volume with spinal fluid amyloid-β and tau," *Frontiers in aging neuroscience*, vol. 5, p. 55, 2013.

[53] M. J. Clarkson, M. J. Cardoso, G. R. Ridgway, M. Modat, K. K. Leung, J. D. Rohrer, N. C. Fox, and S. Ourselin, "A comparison of voxel and surface based

cortical thickness estimation methods," *Neuroimage*, vol. 57, no. 3, pp. 856–865, 2011.

[54] I. Aganj, G. Sapiro, N. Parikshak, S. K. Madsen, and P. M. Thompson, "Measurement of cortical thickness from MRI by minimum line integrals on soft-classified tissue," *Human brain mapping*, vol. 30, no. 10, pp. 3188–3199, 2009.

[55] S. E. Jones, B. R. Buchbinder, and I. Aharon, "Three-dimensional mapping of cortical thickness using Laplace's equation," *Human brain mapping*, vol. 11, no. 1, pp. 12–32, 2000.

[56] S. R. Das, B. B. Avants, M. Grossman, and J. C. Gee, "Registration based cortical thickness measurement," *Neuroimage*, vol. 45, no. 3, pp. 867–879, 2009.

[57] B. Fischl and A. M. Dale, "Measuring the thickness of the human cerebral cortex from magnetic resonance images," *Proceedings of the National Academy of Sciences*, vol. 97, no. 20, pp. 11 050–11 055, 2000.

[58] X. Han, J. Jovicich, D. Salat, A. van der Kouwe, B. Quinn, S. Czanner, E. Busa, J. Pacheco, M. Albert, R. Killiany *et al.*, "Reliability of MRI-derived measurements of human cerebral cortical thickness: the effects of field strength, scanner upgrade and manufacturer," *Neuroimage*, vol. 32, no. 1, pp. 180–194, 2006.

[59] J. P. Lerch and A. C. Evans, "Cortical thickness analysis examined through

power analysis and a population simulation," *Neuroimage*, vol. 24, no. 1, pp. 163–173, 2005.

[60] H. Haidar and J. S. Soul, "Measurement of cortical thickness in 3D brain MRI data: validation of the Laplacian method," *Journal of Neuroimaging*, vol. 16, no. 2, pp. 146–153, 2006.

[61] K. Im, J.-M. Lee, J. Lee, Y.-W. Shin, I. Y. Kim, J. S. Kwon, and S. I. Kim, "Gender difference analysis of cortical thickness in healthy young adults with surface-based methods," *Neuroimage*, vol. 31, no. 1, pp. 31–38, 2006.

[62] N. E. Foster and R. J. Zatorre, "Cortical structure predicts success in performing musical transformation judgments," *Neuroimage*, vol. 53, no. 1, pp. 26–36, 2010.

[63] M. Waehnert, J. Dinse, M. Weiss, M. N. Streicher, P. Waehnert, S. Geyer, R. Turner, and P.-L. Bazin, "Anatomically motivated modeling of cortical laminae," *Neuroimage*, vol. 93, pp. 210–220, 2014.

[64] S. T. Bok, "Der Einflu\der in den Furchen und Windungen auftretenden Krümmungen der Gro\hirnrinde auf die Rindenarchitektur," *Zeitschrift für die gesamte Neurologie und Psychiatrie*, vol. 121, no. 1, p. 682, 1929.

[65] J. T. Ratnanather, S. Arguillère, K. S. Kutten, P. Hubka, A. Kral, and L. Younes, "3D normal coordinate systems for cortical areas," in *Mathemat-*

ics of Shapes and Applications. World Scientific, 2019, vol. 37, ch. 7, pp. 167–180.

[66] Center for Integrative Biomedical Computing, 2016, seg3D: Volumetric Image Segmentation and Visualization. Scientific Computing and Imaging Institute (SCI), Download from: http://www.seg3d.org.

[67] R. Insausti, K. Juottonen, H. Soininen, A. M. Insausti, K. Partanen, P. Vainio, M. P. Laakso, and A. Pitkänen, "MR volumetric analysis of the human entorhinal, perirhinal, and temporopolar cortices," *American journal of neuroradiology*, vol. 19, no. 4, pp. 659–671, 1998.

[68] Krimer, Leonid S and Hyde, TM and Herman, Mary M and Saunders, Richard C, "The entorhinal cortex: an examination of cyto-and myeloarchitectonic organization in humans," *Cerebral cortex*, vol. 7, no. 8, pp. 722–731, 1997.

[69] S. L. Ding and G. W. Van Hoesen, "Borders, extent, and topography of human perirhinal cortex as revealed using multiple modern neuroanatomical and pathological markers," *Human brain mapping*, vol. 31, no. 9, pp. 1359–1379, 2010.

[70] S. Kulason, E. Xu, D. J. Tward, A. Bakker, M. S. Albert, L. Younes, and M. I. Miller, "Entorhinal and transentorhinal atrophy in preclinical Alzheimer's disease," *Frontiers in Neuroscience*, vol. 14, p. 804, 2020.

BIBLIOGRAPHY

[71] R. S. Desikan, F. Ségonne, B. Fischl, B. T. Quinn, B. C. Dickerson, D. Blacker, R. L. Buckner, A. M. Dale, R. P. Maguire, B. T. Hyman *et al.*, "An automated labeling system for subdividing the human cerebral cortex on MRI scans into gyral based regions of interest," *Neuroimage*, vol. 31, no. 3, pp. 968–980, 2006.

[72] A. Maass, D. Berron, L. A. Libby, C. Ranganath, and E. Düzel, "Functional subregions of the human entorhinal cortex," *Elife*, vol. 4, p. e06426, 2015.

[73] S. C. Huntgeburth and M. Petrides, "Morphological patterns of the collateral sulcus in the human brain," *European Journal of Neuroscience*, vol. 35, no. 8, pp. 1295–1311, 2012.

[74] J. Ma, M. I. Miller, A. Trouvé, and L. Younes, "Bayesian template estimation in computational anatomy," *NeuroImage*, vol. 42, no. 1, pp. 252–261, 2008.

[75] S.-W. Cheng, T. K. Dey, and J. Shewchuk, *Delaunay mesh generation*. CRC Press, 2012.

[76] J. Ma, M. I. Miller, and L. Younes, "A bayesian generative model for surface template estimation," *International journal of biomedical imaging*, vol. 2010, 2010.

[77] S. Kulason, M. Miller, and A. Trouvé, "Reaction-diffusion model of cortical atrophy spread during early stages of alzheimer's disease," *bioRxiv*, 2020.

[78] D. Tward and M. Miller, "Unbiased diffeomorphic mapping of longitudinal data

with simultaneous subject specific template estimation," in *Graphs in Biomedical Image Analysis, Computational Anatomy and Imaging Genetics*. Springer, 2017, pp. 125–136.

[79] G. Paxinos and K. B. Franklin, *Paxinos and Franklin's the mouse brain in stereotaxic coordinates*. Academic press, 2019.

[80] H. W. Dong, *The Allen reference atlas: A digital color brain atlas of the C57Bl/6J male mouse*. John Wiley & Sons Inc, 2008.

[81] G. W. van Hoesen, J. C. Augustinack, J. Dierking, S. J. Redman, and R. Thangavel, "The parahippocampal gyrus in Alzheimer's disease: clinical and preclinical neuroanatomical correlates," *Annals of the New York Academy of Sciences*, vol. 911, no. 1, pp. 254–274, 2000.

[82] B. Fischl, A. Van Der Kouwe, C. Destrieux, E. Halgren, F. Ségonne, D. H. Salat, E. Busa, L. J. Seidman, J. Goldstein, D. Kennedy *et al.*, "Automatically parcellating the human cerebral cortex," *Cerebral cortex*, vol. 14, no. 1, pp. 11–22, 2004.

[83] R. K. Olsen, V. A. Carr, A. M. Daugherty, R. La Joie, R. S. Amaral, K. Amunts, J. C. Augustinack, A. Bakker, A. R. Bender, D. Berron *et al.*, "Progress update from the hippocampal subfields group," *Alzheimer's & Dementia: Diagnosis, Assessment & Disease Monitoring*, vol. 11, no. C, pp. 439–449, 2019.

[84] M. I. Miller, J. T. Ratnanather, D. J. Tward, T. Brown, D. S. Lee, M. Ketcha, K. Mori, M.-C. Wang, S. Mori, M. S. Albert, and L. Younes, "Network neurodegeneration in Alzheimer's disease via MRI based shape diffeomorphometry and high-field atlasing," *Front Bioeng Biotechnol*, vol. 3, p. 54, 2015.

[85] S. Kulason, D. J. Tward, T. Brown, C. S. Sicat, C.-F. Liu, J. T. Ratnanather, L. Younes, A. Bakker, M. Gallagher, M. Albert *et al.*, "Cortical thickness atrophy in the transentorhinal cortex in mild cognitive impairment," *NeuroImage: Clinical*, vol. 21, p. 101617, 2019.

[86] T. Nichols and S. Hayasaka, "Controlling the familywise error rate in functional neuroimaging: a comparative review," *Statistical methods in medical research*, vol. 12, no. 5, pp. 419–446, 2003.

[87] X. Tang, M. I. Miller, and L. Younes, "Biomarker change-point estimation with right censoring in longitudinal studies," *The annals of applied statistics*, vol. 11, no. 3, p. 1738, 2017.

[88] L. Younes, M. Albert, and M. I. Miller, "Inferring changepoint times of medial temporal lobe morphometric change in preclinical Alzheimer's disease," *NeuroImage: Clinical*, vol. 5, pp. 178–187, 2014.

[89] D. J. Tward, "Singular geodesic coordinates for representing diffeomorphic maps in computational anatomy, with application to the morphometry of early

Alzheimer's disease in the medial temporal lobe," Ph.D. dissertation, Johns Hopkins University, 2017.

[90] J.-P. Fortin, N. Cullen, Y. I. Sheline, W. D. Taylor, I. Aselcioglu, P. A. Cook, P. Adams, C. Cooper, M. Fava, P. J. McGrath *et al.*, "Harmonization of cortical thickness measurements across scanners and sites," *Neuroimage*, vol. 167, pp. 104–120, 2018.

[91] H. Braak, I. Alafuzoff, T. Arzberger, H. Kretzschmar, and K. Del Tredici, "Staging of Alzheimer disease-associated neurofibrillary pathology using paraffin sections and immunocytochemistry," *Acta Neuropathol*, vol. 112, no. 4, pp. 389–404, 2006.

[92] M. L. Neal and R. Kerckhoffs, "Current progress in patient-specific modeling," *Briefings in bioinformatics*, vol. 11, no. 1, pp. 111–126, 2009.

[93] C. Hogea, C. Davatzikos, and G. Biros, "An image-driven parameter estimation problem for a reaction–diffusion glioma growth model with mass effects," *Journal of mathematical biology*, vol. 56, no. 6, pp. 793–825, 2008.

[94] K. C. Kosel, G. W. Van Hoesen, and D. L. Rosene, "A direct projection from the perirhinal cortex (area 35) to the subiculum in the rat," *Brain Research*, vol. 269, no. 2, pp. 347–351, 1983.

[95] D. C. McIntyre, M. E. Kelly, and W. A. Staines, "Efferent projections of the

anterior perirhinal cortex in the rat," *Journal of Comparative Neurology*, vol. 369, no. 2, pp. 302–318, 1996.

[96] J. L. Guo and V. M. Lee, "Cell-to-cell transmission of pathogenic proteins in neurodegenerative diseases," *Nature medicine*, vol. 20, no. 2, pp. 130–138, 2014.

[97] S. Fornari, A. Schäfer, E. Kuhl, and A. Goriely, "Spatially-extended nucleation-aggregation-fragmentation models for the dynamics of prion-like neurodegenerative protein-spreading in the brain and its connectome," *Journal of Theoretical Biology*, p. 110102, 2019.

[98] A. Mudher, M. Colin, S. Dujardin, M. Medina, I. Dewachter, S. M. A. Naini, E.-M. Mandelkow, E. Mandelkow, L. Buée, M. Goedert *et al.*, "What is the evidence that tau pathology spreads through prion-like propagation?" *Acta Neuropatholog*, vol. 5, no. 1, p. 99, 2017.

[99] S. B. Prusiner, "Novel proteinaceous infectious particles cause scrapie," *Science*, vol. 216, no. 4542, pp. 136–144, 1982.

[100] A. Aguzzi, C. Sigurdson, and M. Heikenwaelder, "Molecular mechanisms of prion pathogenesis," *Annu. Rev. Pathol. Mech. Dis.*, vol. 3, pp. 11–40, 2008.

[101] A. Aguzzi and L. Rajendran, "The transcellular spread of cytosolic amyloids, prions, and prionoids," *Neuron*, vol. 64, no. 6, pp. 783–790, 2009.

[102] M. Jucker and L. C. Walker, "Self-propagation of pathogenic protein aggregates in neurodegenerative diseases," *Nature*, vol. 501, no. 7465, pp. 45–51, 2013.

[103] M. Schöll, S. N. Lockhart, D. R. Schonhaut, J. P. ONeil, M. Janabi, R. Ossenkoppele, S. L. Baker, J. W. Vogel, J. Faria, H. D. Schwimmer *et al.*, "PET imaging of tau deposition in the aging human brain," *Neuron*, vol. 89, no. 5, pp. 971–982, 2016.

[104] R. Ossenkoppele, D. R. Schonhaut, M. Schöll, S. N. Lockhart, N. Ayakta, S. L. Baker, J. P. ONeil, M. Janabi, A. Lazaris, A. Cantwell *et al.*, "Tau PET patterns mirror clinical and neuroanatomical variability in Alzheimers disease," *Brain*, vol. 139, no. 5, pp. 1551–1567, 2016.

[105] K. Tagai, M. Ono, M. Kubota, S. Kitamura, K. Takahata, C. Seki, Y. Takado, H. Shinotoh, Y. Sano, Y. Yamamoto *et al.*, "High-contrast in vivo imaging of tau pathologies in alzheimers and non-alzheimers disease tauopathies," *Neuron*, 2020.

[106] M. P. Witter, T. P. Doan, B. Jacobsen, E. S. Nilssen, and S. Ohara, "Architecture of the entorhinal cortex a review of entorhinal anatomy in rodents with some comparative notes," *Frontiers in Systems Neuroscience*, vol. 11, p. 46, 2017.

[107] A. Kobro-Flatmoen and M. P. Witter, "Neuronal chemo-architecture of the

entorhinal cortex: A comparative review," *European Journal of Neuroscience*, vol. 50, no. 10, pp. 3627–3662, 2019.

[108] L. Xie, J. B. Pluta, S. R. Das, L. E. Wisse, H. Wang, L. Mancuso, D. Kliot, B. B. Avants, S.-L. Ding, J. V. Manjón *et al.*, "Multi-template analysis of human perirhinal cortex in brain MRI: Explicitly accounting for anatomical variability," *NeuroImage*, vol. 144, pp. 183–202, 2017.

Curriculum Vitae

Sue Kulason was born in New York, New York in 1991. She graduated from Johns Hopkins University with a Bachelor of Science in Biomedical Engineering and a minor in Computer Integrated Surgery in 2013. She then enrolled in the Johns Hopkins School of Medicine Biomedical Engineering Doctorate program and joined the Center for Imaging Science under the supervision of Michael Miller. In 2015, she won a Fulbright Fellowship and Whitaker Scholarship to conduct research at the Applied Mathematical Institute at École Normale Supérieure de Paris-Saclay under the supervision of Alain Trouvé. She continued her mathematical education in tandem with her doctorate research at Johns Hopkins University. Sue graduated with a Master of Science in Applied Mathematics and Statistics in 2019, then graduated with a Doctorate of Philosophy in Biomedical Engineering in 2020.